Elastic Contractile Stress in the Basement Membrane Generates Basal Tension in Epithelia

K. Yanín Guerra Santillán [1,2] Christian Dahmann [2,1,*] and Elisabeth Fischer-Friedrich [1,2,3,*]

[1] *Cluster of Excellence Physics of Life, Technische Universität Dresden, Dresden, Germany*

[2] *School of Science, Technische Universität Dresden, Dresden, Germany*

[3] *Biotechnology Center, Technische Universität Dresden, Dresden, Germany*

(Received 11 August 2023; accepted 11 December 2023; published 23 January 2024)

The shaping of epithelial tissues into functional organs often depends on dynamic changes of mechanical tension at the apical and basal sides of cells. While on the apical side, tension is known to be regulated by the apical actomyosin meshwork, basal tension regulation remains elusive due to the presence of a basal sheet of specialized extracellular matrix, the basement membrane. Here, we use atomic force microscopy to provide direct measurements of mechanical tension in the basal surface of the wing disk epithelium of *Drosophila* in control and perturbed conditions. We find that next to actomyosin, the basement membrane is a key structure for the generation of basal tension. Furthermore, we show that the basement membrane is a solidlike sheet subject to an expansile stretch in epithelial homeostasis. Performing osmotic shocks and optogenetic actomyosin activation, we find evidence that basal stretch and tension can be generated by intracellular hydrostatic pressure and actomyosin tension in lateral cell faces of the epithelium. In conclusion, we propose that elastic contractile stress corresponding to the actomyosin-induced expansile stretch of the basement membrane generates a major contribution to basal tension. We thereby disclose fundamental differences in the mechanical regulation of apical and basal epithelial tension.

DOI: 10.1103/PRXLife.2.013004

I. INTRODUCTION

The body of all animals is to a large extent composed of epithelial cell sheets [1]. Epithelia consist of polarized cells and, correspondingly, exhibit two distinct outer tissue surfaces referred to as apical and basal surfaces. The basal surface of cells is connected to a basement membrane composed of extracellular matrix (ECM) proteins [2], among which collagen IV was shown to be particularly crucial for its mechanical integrity [3–5]. During embryogenesis, epithelia need to undergo complex shape changes to attain their final and functional shape. The basement membrane was described to be important in this process [3,6–8]. Epithelial shape changes are often driven by asymmetries in apical and basal cell surface tension [9]. Therefore, understanding the regulation of apical and basal tension in epithelia is crucial to understand and engineer tissue shape in organoids or developing animals. Research on the mechanical forces that drive epithelial sheet movements has been mainly focused on the generation of apical tension by the actomyosin cytoskeleton [10]. By contrast, the specific contributions of the basement membrane in the generation of basal tension in epithelial tissues have been mostly disregarded and remain unclear [11].

The developing *Drosophila* wing disk epithelium is a pervasive model to understand epithelial shape changes during development. It is a single-cell layered epithelium which gives rise to the future wing blade, notum, and hinge of the adult fly [12]. The basement membrane of the wing disk was shown to play an important role during the morphogenesis of this tissue [13–16] and several studies [15–17] have suggested that there is an elastic stretch in the basement membrane that could give rise to a passive mechanical tension. However, an experimental verification of this hypothesis through direct mechanical measurements is still lacking.

Many previous studies on *Drosophila* tissue mechanics estimate cellular surface tension in terms of recoil velocities of cut cell edges after application of laser cuts to lateral cell faces [15,18,19]. Such tension measurements are indirect mechanical measurements and rely on the assumption that friction coefficients are constant. Corresponding tension estimates are in the following referred to as "edge tensions." Basal edge tensions were previously reported as edge tensions measured in the vicinity of the basal surface but not at the basal surface itself [15].

Here, we provide direct measurements of mechanical tension in the basal surface of the wing disk epithelium using atomic force microscopy. Employing molecular perturbations, we identify both the basement membrane and the actomyosin network as important structural components in basal tension generation. Furthermore, we show that the basement membrane contributes to contractile tension generation while actomyosin induces an expansile stress in basal cell faces. Using live imaging of explanted wing disks, we show that collagen IV turnover and mobility in the wing disk are slow, indicating solidlike material properties. This leads us to the

*Corresponding authors: christian.dahmann@tu-dresden.de; elisabeth.fischer-friedrich@tu-dresden.de

hypothesis that an expansile stretch of the basement membrane and a corresponding elastic stress are key to basal tension generation in epithelial homeostasis. Furthermore, we show that induced changes of the basal surface area through optogenetic activation of lateral actomyosin or osmotic shocks triggers proportional changes in basal tension. Finally, we provide a model of cellular force balances to rationalize how active intracellular processes can maintain elastic basement membrane stretch in epithelial homeostasis.

II. RESULTS

A. Basal tension depends on the basement membrane and on the actomyosin cytoskeleton

To probe the mechanical properties of the basal surface of the wing disk, we performed shallow indentations with the pyramidal indenter of the cantilever of an atomic force microscope (AFM) [see Figs. 1(a) and 1(b) and Materials and Methods, Sec. IV C]. As a readout, we obtained force-indentation curves [see Fig. 1(c)], showing the rise of measured AFM force F in dependence of cantilever tip indentation δ. Performing indentation experiments after digestion of the basement membrane with collagenase (see Materials and Methods), we observed that the material was substantially softened (see Fig. S1(a) of the Supplemental Material [20]). Correspondingly, we inferred that the mechanical response of the tissue was dominated by the thin basement membrane layer at the basal surface rather than the cytoplasmic bulk. Furthermore, we and others found evidence that the basement membrane is subject to mechanical tension judged by area changes upon collagenase treatment and actomyosin perturbation (see Figs. 1(i)–1(k) and, e.g., Ref. [15]). Accordingly, we concluded that the force curves in our experiments were best described by a theoretical model describing the indentation of a tensed thin sheet [23]. The choice of the tensed-sheet model is further corroborated by our observation that force-indentation curves are approximately linear (see Sec. IV G of Materials and Methods for a detailed discussion). We adapted an analysis scheme that was previously established for the measurement of apical surface tension in mammalian cells and cell wall tension in plant cells [23–26]. Correspondingly, we estimated basal tension in the wing disk as $\sigma_b = F'_{\mathrm{lin}}/\pi$ throughout this paper, where F'_{lin} is the fitted linear slope of the measured force-indentation curve [see Fig. 1(c) and Materials and Methods). Since we present here to our best knowledge the first study of basal tension measurements through AFM indentation, we encourage the interested reader to review our detailed discussion of this method and the justification of its applicability in Sec. IV G of Materials and Methods. We find that obtained basal tension values are in the range 0.2–0.5 mN/m for wing discs explanted 72 h after egg lay [AEL; see Figs. 1(d)–1(h)]. Therefore, tension values closely matched values of actin cortical tension measured in interphase cells via micropipette aspiration or AFM measurements [27–30].

Since the basal cell face is a structural composite of a thin actomyosin film (inner side of the plasma membrane) and the basement membrane layer (outer side of the plasma membrane), basal tension may depend on both the basement membrane and/or the actomyosin cytoskeleton. To test this hypothesis, we first explanted wing disks 72 h AEL and treated them with collagenase, which degrades the basement membrane [3]. Collagenase treatment resulted in a reduction of basal tension estimates by ≈60% (Fig. 1(d) and Supplemental Material Fig. S2(a) [20]). We note that tension values determined in the situation of digested basement membrane present an upper bound of the remnant basal tension. This is due to the treatment-induced increasing influence of cytoplasm stiffness in AFM indentation which may give rise to tension overestimation (see Sec. IV G). Correspondingly, basal tension likely drops even more through collagenase treatment than reported by our quantitative analysis in Fig. 1(d).

Next, we perturbed the actomyosin cytoskeleton. Treatment of explanted wing disks with the Rho kinase (Rock) inhibitor Y27632 reduced basal tension by ≈30% (Fig. 1(e) and Supplemental Material Fig. S2(b) [20]). Incubation with Latrunculin A—an inhibitor of actin polymerization—resulted in a reduction of basal tension by ≈55% (Fig. 1(f) and Supplemental Material Fig. S2(c) [20]). As a control experiment, we verified that incubation of wing disks in 4% PBS and 0.1% DMSO did not significantly change basal tension [Figs. 1(g) and 1(h)].

In order to rule out that basal tension reduction upon collagenase treatment was due to a concomitant decrease in actomyosin contractility, we monitored the time evolution of fluorescently labeled myosin II (Sqh-GFP) at the basal side upon addition of collagenase. We find no concomitant decrease of myosin II at the basal side but instead a shallow transient increase (see Supplemental Material Figs. S2(d)–S2(f) [20]). That finding supports our conclusion that tension reduction is due to the change of the basement membrane itself and not by an indirect effect on myosin II. Taken together, our data give evidence that the actomyosin cytoskeleton and the basement membrane contribute both to the generation of basal tension.

In addition, we monitored the change of apical and basal cell areas in response to treatments with the above-mentioned reagents. None of the reagents changed apical cell areas significantly [see Figs. 1(i)–1(k), and Figs. S2(g)–S2(i) and S5, two top rows in each panel field]. For basal cell areas, we interestingly found opposite changes in response to collagenase and actomyosin-perturbing drugs. While collagenase treatment led to a median increase of basal cell areas of ≈18%, the Rock inhibitor Y27632 and Latrunculin A both reduced basal cell areas by ≈5% and 12%, respectively [see Figs. 1(i)–1(k) and Figs. S2(g)–S2(i) and S5, two bottom rows in each panel field]. We conclude that tension reduction upon collagenase-induced basement membrane degradation is linked to basal widening. However, basal tension reduction through deactivation of actomyosin contractility is connected to basal shrinkage.

B. Basal tension depends on developmental time and wing disk position

The spatiotemporal control of mechanical tension contributes to epithelial morphogenesis [31–33]. We therefore next tested whether basal tension depended on developmental time and/or position within the wing disk. Wing disks are relatively flat structures until a developmental time point of

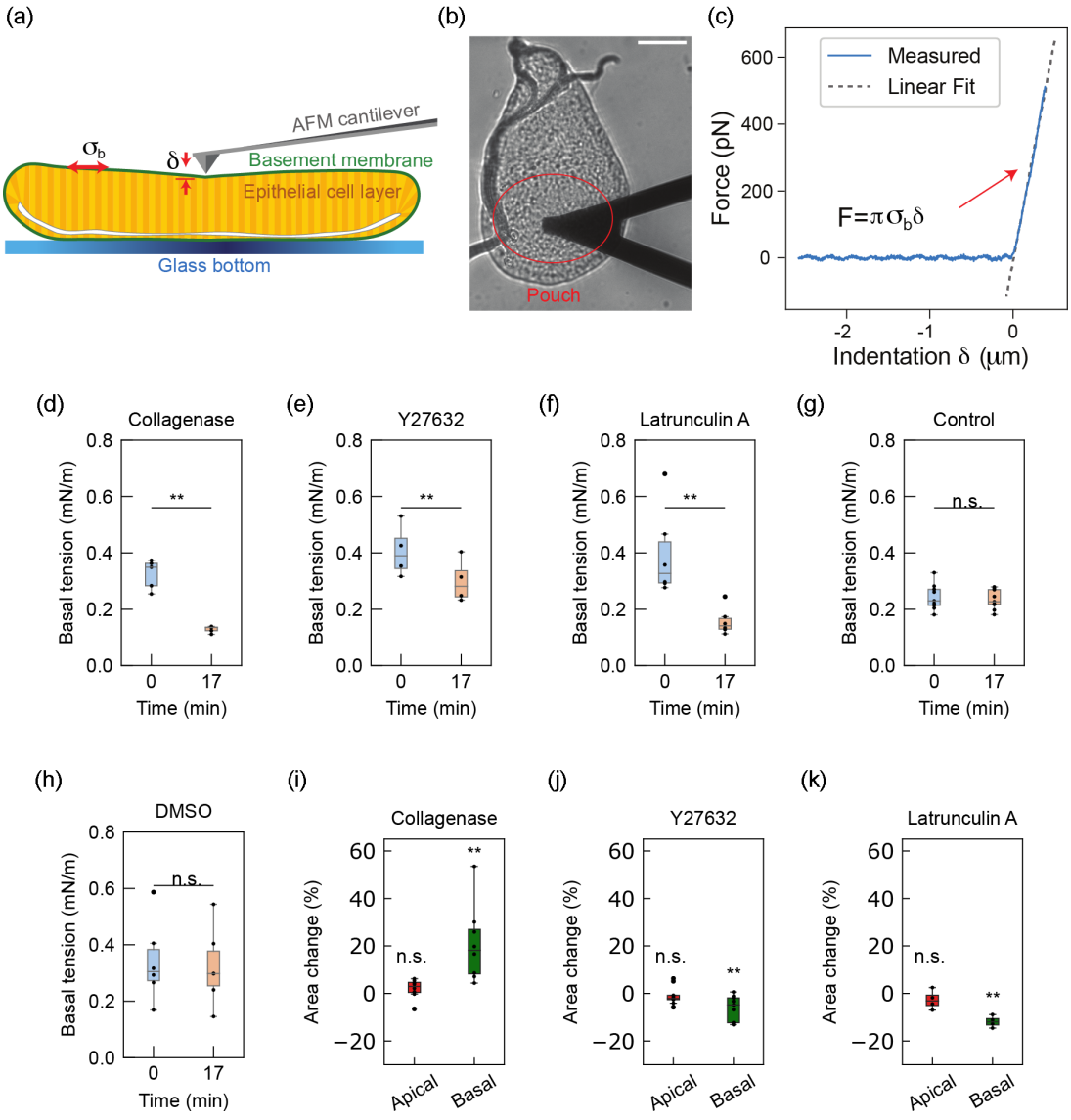

FIG. 1. Basal tension depends on the basement membrane and on the actomyosin cytoskeleton. (a) Schematic illustrating the measurement of basal tension (σ_b) of wing disks. The force applied by an AFM cantilever results in the indentation (δ) of the basal surface. (b) Brightfield micrograph of an explanted wing disk during an AFM measurement. Scale bar: 50 μm. (c) Exemplary force-indentation curve recorded by the AFM during the lowering of the cantilever over the tissue. The force F starts to increase approximately linearly after the cantilever has touched the tissue surface. A linear fit is shown by the dashed line. The magnitude of the linear slope divided by π is used as an estimate of basal tension. [(d)–(h)] Boxplots showing basal tension estimates measured in the central pouch region of 72 h AEL wing disks before (0 min) and after 17 min incubation with indicated reagents (collagenase. 0.2 mg/ml, $N = 5$; Y27632, 1 mM, $N = 4$; Latrunculin A, 4 μM, $N = 6$ with one outlier outside plot's range; control, 4% PBS, DMSO 0.1%, $N = 6$). [(i)–(k)] Boxplots indicating changes of apical and basal cell areas upon 17 min incubation with indicated reagents [collagenase, $N = 8$; Y27632, $N = 9$; Latrunculin A, $N = 5$, same concentrations as in (d)–(f)]. For panels (d)–(h), statistical significance of differences between basal tension before and after treatment was determined with a paired t-test. For panels (i)–(k), each distribution (apical and basal area changes) was tested with a one-sample t-test (two-tailed) against the null hypothesis that the data stem from a normal distribution with mean equal to zero ($^{*}p < 0.05$, $^{**}p < 0.01$, $^{***}p < 0.001$, n.s., not significant).

≈72 h AEL. Thereafter, three stereotypic folds form in the hinge region of the wing disk [see Fig. 2(a)]. We therefore probed basal tension in a developmental time window around fold initiation at 64, 68, 72, 76, and 80 h AEL. (The central hinge fold starts to emerge at approximately 72 h AEL. This fold will be subsequently referred to as H/H fold.) We noted that once the tissue was folded, meaningful tension measurements in the hinge region were not possible anymore. Therefore, we decided to measure basal tension mainly in the pouch region for this analysis. Basal tension was relatively low at 64 h AEL, significantly increased by 68 h AEL, and thereafter declined to reach a value at 76 and 80 h AEL similar to the one at 64 h AEL [see Fig. 2(b)]. Thus, the basal surface in the pouch region of the epithelium becomes increasingly tensed right before the onset of fold formation and relaxes mechanically during the time period of fold formation. We note that previous work using laser cutting in the lateral cell surface close to the basal surface reported

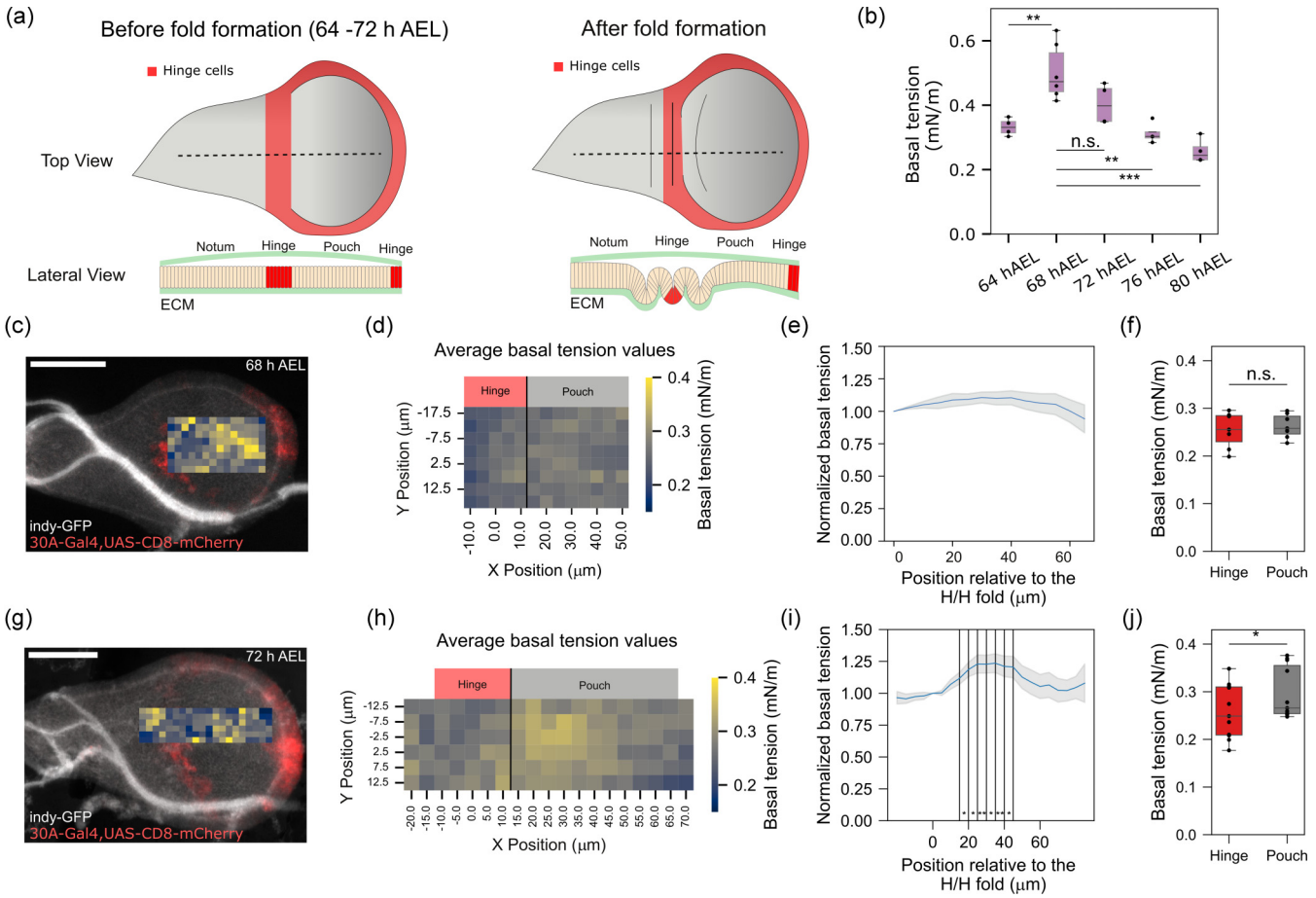

FIG. 2. Basal tension depends on developmental time and wing disk position. (a) Schematics of top views and lateral views of wing disks before and after fold formation. (b) Boxplot of basal tension in the pouch center at the indicated stages of development: 64 h AEL ($N = 4$ wing disks), 68 h AEL ($N = 5$), 72 h AEL ($N = 4$), 76 h AEL ($N = 6$), and 80 h AEL ($N = 4$). Significance was determined with a Mann-Whitney U-test. [(c)–(j)] Basal tension measured across different regions of the wing disk at [(c)–(f)] 68 h AEL and [(g)–(j)] 72 h AEL. [(c), (g)] Confocal image of measured wing disks expressing Indy-GFP to visualize cell membranes (gray; the bright structures are autofluorescent tracheae) and 30A-Gal4,UAS-CD8-mCherry (red), specifically labeling the prospective H/H fold cells. The overlying heat maps show the basal tension (raw data, no smoothing) measured in a rectangular grid with pixel edge length 5 μm along the wing disk, respectively. Scale bars: 50 μm. [(d), (h)] Heat maps showing the average measured basal tension over several (d) 68 h AEL and (h) 72 h AEL wing disks with quantitative scales. We note that the extension of AFM scan regions was limited by the presence of the trachea on the surface of the wing disk (68 h AEL, $N = 7$; 72 h AEL, $N = 10$). [(e), (i)] Mean and standard error of the mean (s.e.m.) of the normalized basal tension along the wing disk long axis (X axis) relative to the prospective H/H fold cells for $N = 7$ and $N = 11$ wing disks, respectively. Tension was normalized by the tension value of the prospective H/H fold cells ($X = 0$ position). Significance stars in the plot indicate that normalized tension values at the corresponding X position (indicated by vertical line) are statistically different from one, i.e., in relative terms different from the tension in the H-H fold (bin size 5 μm). Significance was determined with a one-sample t-test (two-tailed) against the null hypothesis that the data come from a normal distribution with a mean equal to one. [(f), (j)] Boxplots of the median basal tension measured in the hinge region [≈25 μm extension as shown in (d) and (h)] and in the pouch region [≈45 μm extension as shown in (d) and (h)] of (f) 68 h AEL and (j) 72 h AEL wing disks. Statistical significance of differences between basal tension in the hinge and in the pouch region was determined with a paired t-test ($^{*}p < 0.05$, $^{**}p < 0.01$, $^{***}p < 0.001$, n.s., not significant).

an increase of inferred basal edge tension in the wing disk pouch at a similar time point in development [15]. Therefore, the time-evolution trend of this basal edge tension appeared to be opposite to the here-reported AFM-measured basal tension.

Next, we investigated the dependence of basal tension on the position within the wing disk. To this end, we performed a series of indentations along a spatial grid covering a region from the hinge to the pouch at two different developmental time points, before (68 h AEL) and at the onset of H/H fold formation (72 h AEL) [see Figs. 2(c)–2(j)]. To align the measurements from different wing disks, the grids were positioned relative to the prospective H/H fold cells, as identified by the activity of the 30A-Gal4 line as visualized by the expression of CD8-mCherry shown in red [see Figs. 2(c) and 2(g)]. At 68 h AEL, the hinge and the pouch region exhibited comparable basal tensions [see Figs. 2(d)–2(f)]. By contrast, at 72 h AEL, basal tension was significantly higher (by ≈25%) in the pouch region compared to the H/H fold region [see Figs. 2(h)–2(j)]. In conclusion, our results show that slight spatial variations in basal stress occur coincident with the onset of fold formation.

C. Long-term imaging of collagen IV suggests solidlike properties of the basement membrane

We next explored the physical mechanisms that contribute to basal tension in the wing disk. Based on our observation that basal tension depends critically on collagen IV and, thus, on the integrity of the basement membrane, we hypothesized that basal tension could be, at least in part, generated through elastic stretch of the basement membrane as was put forward in previous research [15]. However, this hypothesis relies on a solidlike behavior of the basement membrane in the sense that it can store deformation-induced stresses long term like an elastic solid rather than dissipating respective stresses quickly like a viscous fluid [34]. (We note that the long-term storage of stresses requires the presence of a nonvanishing storage modulus in the relevant frequency range but does not require a vanishing corresponding loss modulus. In other words, viscous dissipation may be present in addition.)

We know from previous research that the basement membrane is a cross-linked biopolymer network that can store elastic stresses short term (see, e.g., Refs. [3,35]). However, molecular turnover leads to the dissipation of elastic stresses (and a corresponding decline of the storage modulus) on timescales of material turnover (see, e.g., Refs. [29,36–38]). To estimate the corresponding turnover timescales of the basement membrane, we decided to measure the turnover dynamics of the basement membrane material, namely, collagen IV.

As collagen IV is produced in the larval fat body [13], i.e., outside of the wing disk, collagen turnover in explanted wing disks can be quantified by the monitoring of collagen IV intensity decrease over time. We measured collagen IV using the ColIVα2::GFP exon trap line (hereafter ColIV-GFP) [39]. Wing disks were explanted at 72 h AEL and ColIV-GFP was imaged for 7 h at the basal side of the pouch and notum/hinge regions [see Figs. 3(a)–3(e)]. Within this time, ColIV-GFP intensity decayed by only $\approx$20% in both pouch and notum/hinge region [see Figs. 3(c) and 3(d)]. To obtain an estimate of collagen IV turnover timescales, we fitted an exponential decay function to ColIV-GFP intensity over time. As a result, we found characteristic decay times on the order of 30 h [see Figs. 3(d) and 3(e)].

To further test the mobility and turnover of collagen IV in the wing disk basement membrane, we also performed fluorescence recovery after photobleaching (FRAP) experiments on the basement membrane of explanted wing disks expressing ColIV-GFP [see Figs. 3(f)–3(h)]. Long-term imaging of photobleached areas revealed that there was very little or no recovery of ColIV-GFP fluorescence [below 5% in 7 h after bleaching; see Fig. 3(h)]. In addition, the bleached fluorescence intensity profile stayed largely intact over 7 h, indicating that there was little or no mobility of collagen IV molecules in the basement membrane [Fig. 3(i)].

Taken together, our experiments of long-term imaging and photobleaching of ColIV-GFP in the basal side of the wing disk indicate that the turnover and mobility of collagen IV in the basement membrane are slow as compared to morphogenetic timescales such as fold formation, i.e., a few hours [15]. In conjunction with our finding that basal tension estimates are not significantly altered by slowed indentation speed (see Fig. S4), this indicates that the basement membrane material can be described as an elastic material since it is in the rubber plateau of entangled biopolymer networks [40]. Therefore, we conclude that from the perspective of morphogenetic tissue changes such as epithelial folding in the wing disk, the basement membrane can be considered as a solidlike elastic material in that it can store elastic stresses.

D. Optogenetic activation of lateral actomyosin contractility increases basal cell areas and tension

Given our experimental results in support of the solidlike nature of the basement membrane in combination with our finding of a strong influence of collagen IV on measured basal tension [Figs. 1(d) and 3], we further wanted to consolidate the idea that elastic stretch of the basement membrane might be an important contribution to basal tension in the epithelium. The elastic stretch of the basement membrane corresponds to an increase of basal tension by a passive stretch-induced contribution $K_b(\mathcal{A}_b - \mathcal{A}_0)/\mathcal{A}_0$ in addition to an active actomyosin-based contribution σ_b^{act}. Here, K_b is an elastic area bulk modulus of the basal cell surface, $\mathcal{A}_b$ is the basal cell surface area, and $\mathcal{A}_0$ is the resting basal cell surface area in the absence of stress. Therefore, our hypothesis predicts that basal tension increases further by external perturbations that enlarge basal stretch.

To test this prediction experimentally, we augmented lateral tension by optogenetic recruitment of RhoGEF2, an activator of actomyosin contractility [41], to the lateral surfaces of wing disk pouch cells [see Figs. 4(a)–4(e)]. Optogenetic recruitment was based on the light-dependent binding of cryptochrome 2 (Cry2) fused to RhoGEF2 (RhoGEF2-Cry2) to the N-terminal region of CIB protein (NCIB), which was targeted by a CaaX anchor to the plasma membrane (see Refs. [42,43]). We previously showed using this optogenetic activation that recruitment of RhoGEF2 to the lateral plasma membrane of wing disk cells results in localized lateral accumulation of F-actin, increased lateral tension, and decreased apical-basal cell height [43].

As previously described [43], we illuminated a "lateral" volume of wing disk pouch cells using two-photon excitation with a pulsed laser of wavelength $\lambda = 950$ nm for 2 min [see Figs. 4(a) and 4(b)]. Right after the end of photoactivation, epithelial cell height was decreased by $\approx$9%, indicating that lateral tension was increased [see Figs. 4(e) and 4(f)]. Concomitant with the decrease in cell height, both apical and basal cell surface areas were increased by $\varepsilon_a \approx 15.4\%$ and $\varepsilon_b \approx 7\%$, respectively [see Figs. 4(c), 4(d), and 4(f)]. Over time, cell shapes relaxed back to their original shape with a complete relaxation after $\approx$10 min, consistent with our previously reported observations [43]. To test whether the increase in basal cell area influences basal tension, we again illuminated cells with light of wavelength $\lambda = 950$ nm for 2 min and used AFM indentation to measure basal tension at different time points after the end of illumination. Basal tension was increased by $\Delta\tilde{\sigma}_b \approx 15.5\%$ right after optogenetic activation and thereafter declined within $\approx$4 min to the level before activation [see Fig. 4(g)]. Thus, as predicted by our model, basal tension can be increased through an increase in basal stretch. Taken together, our data demonstrate that

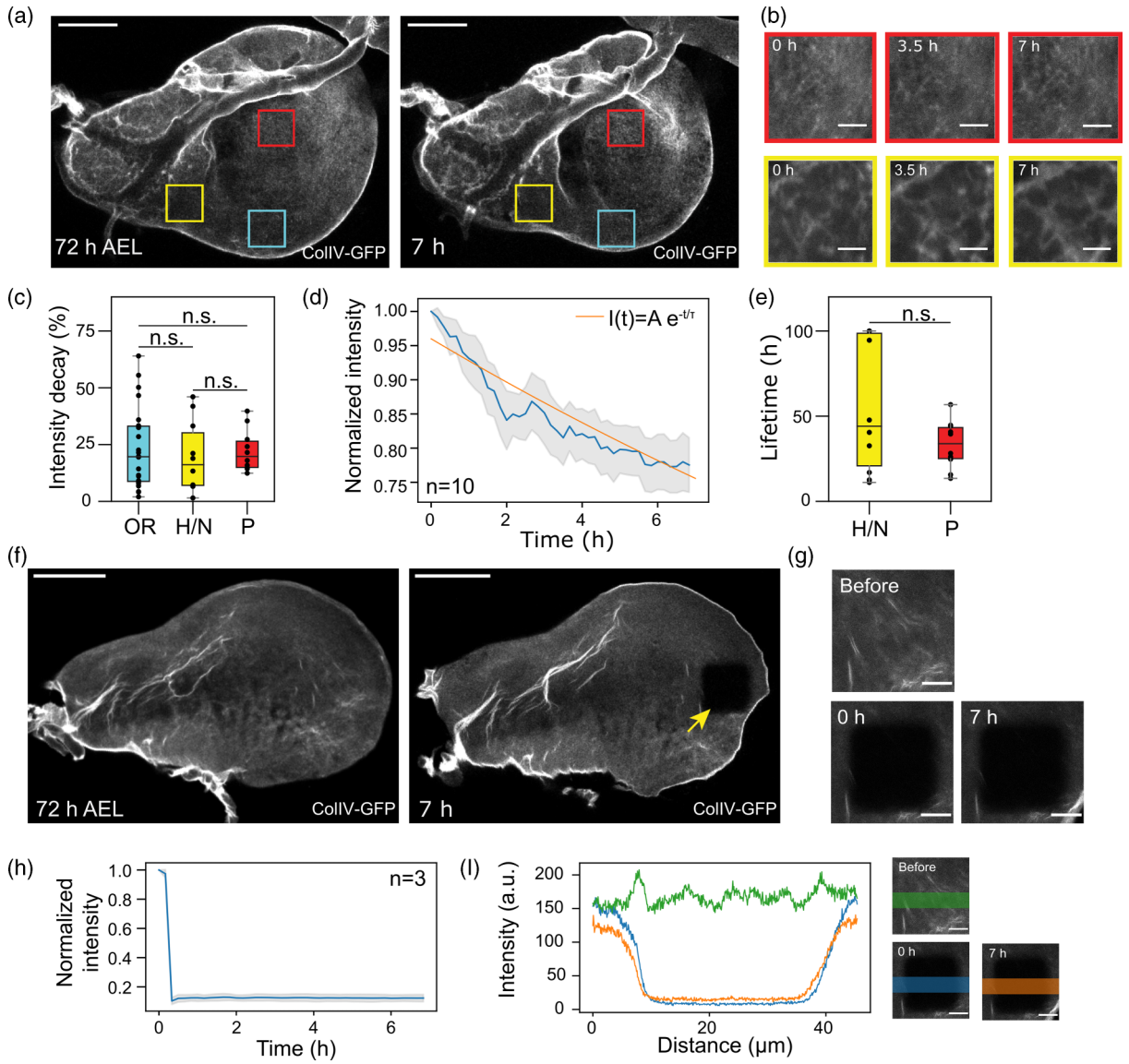

FIG. 3. Long-term imaging of collagen IV suggests solidlike properties of the basement membrane. (a) Sum fluorescence intensity projections of a Z stack of images of the basal side of a 72 h AEL wing disk expressing ColIV-GFP freshly mounted (left panel) and 7 h in culture. The regions indicated by the yellow and red 30×30 μm^2 squares were imaged every 10 min for 7 h [yellow, hinge or notum (H/N); red, pouch (P)]. The cyan 30×30 μm^2 square was only imaged at $t = 0$ h and 7 h as a photobleaching control. This region is labeled as outside region of interest (OR). Scale bars: 50 μm. (b) Magnified views of the regions indicated in (a) by the red and yellow squares at the indicated time points. Scale bars: 10 μm. (c) Boxplot of ColIV-GFP fluorescence intensity decay between $t = 0$ h and $t = 7$ h in different regions of the wing disk as indicated in panel (a). (d) Normalized ColIV-GFP fluorescence intensity over time of pouch-located 30×30 μm^2 squares averaged over ten wing disks (blue line). The fluorescence intensity was normalized by the initial value of each wing disk. The grey area indicates the standard error of the mean. An exponential decay is fitted (orange line) with decay time $\tau = 27.2$ h. (e) Boxplot of lifetime of ColIV-GFP in the pouch (P) and hinge/notum (H/N) regions of wing disks ($N = 10$ wing disks, each). (f) Sum fluorescence intensity projections of a Z stack of images of the basal part of a 72 h AEL wing disk expressing ColIV-GFP. Left: Freshly mounted wing disk before photobleaching. Right: 7 h after photobleaching. The yellow arrow indicates the position of the 30×30 μm^2 square that was bleached and subsequently imaged every 10 min. Scale bars: 50 μm. (g) Images of the bleached area before bleaching and at time points $t = 0$ h and $t = 7$ h, respectively. Scale bars: 10 μm. (h) Normalized mean ColIV-GFP fluorescence intensity over time after photobleaching averaged over three wing disks (blue line). The grey area indicates the standard error of the mean. Normalized as in (d). (i) ColIV-GFP fluorescence intensity along a horizontal line scan overlapping a photobleached region (see panels on the right) before bleaching and at time points $t = 0$ h and $t = 7$ h, respectively. For panels (c) and (e), significance was determined with a Mann-Whitney U-test ($^*p < 0.05$, $^{**}p < 0.01$, $^{***}p < 0.001$, n.s., not significant).

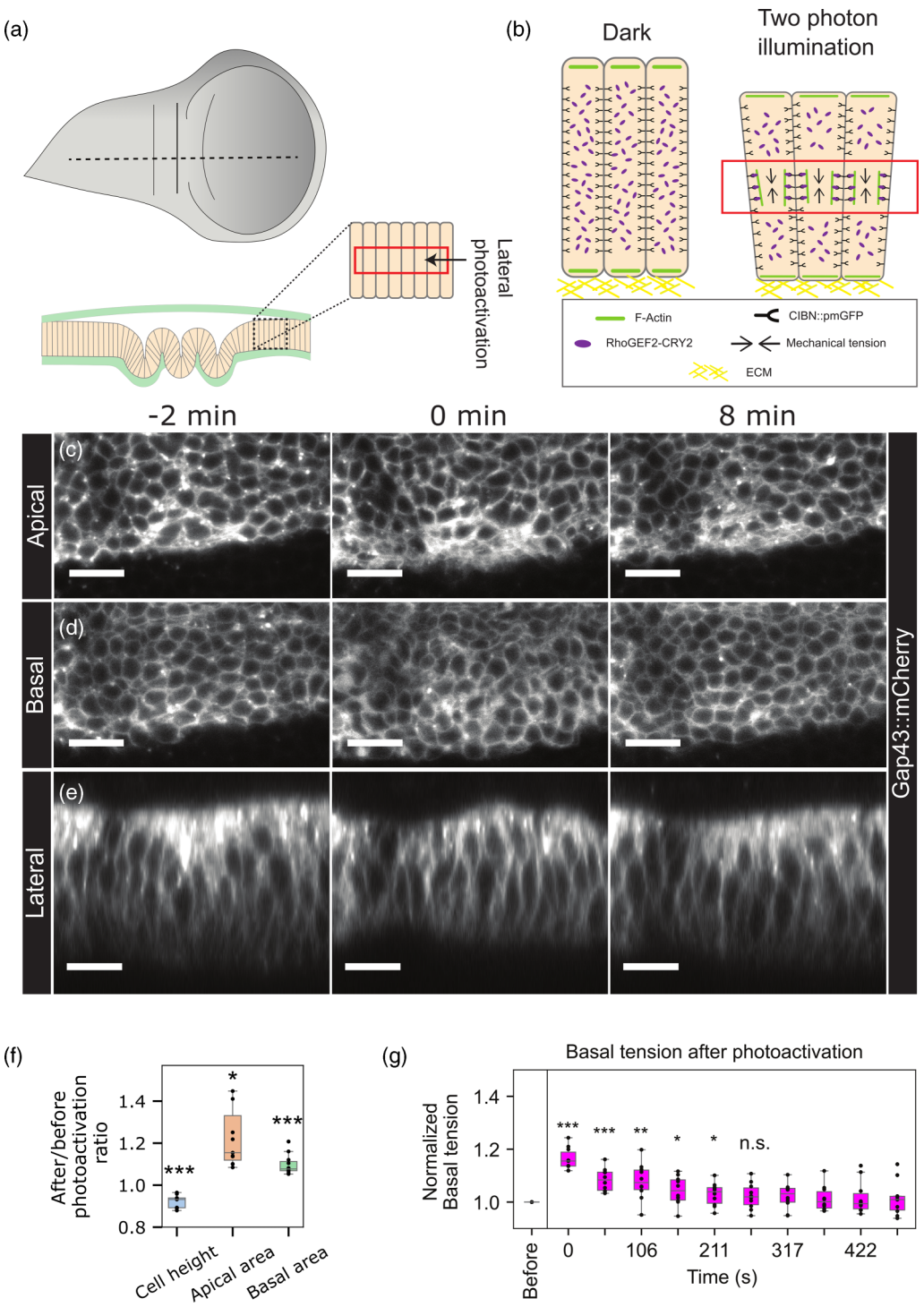

FIG. 4. Basal tension is increased by optogenetic activation of lateral actomyosin contractility. (a) Schematic illustrating the region of the wing disk that was illuminated for lateral photoactivation. The red area indicates the cross-section view of 15 planes, 1 μm apart, that were continuously illuminated for 2 min with light of wavelength $\lambda = 950$ nm. (b) Cartoon illustrating the distribution of the Rho1 activator RhoGEF2-CRY2 (purple) before and after 2 min of two-photon excitation. In the dark condition, RhoGEF2-CRY2 is localized in the cytoplasm (left). Upon two-photon excitation, RhoGEF2-CRY2 binds to CIBN::pmGFP, which localizes to the plasma membrane (right). Once at the plasma membrane, RhoGEF2-CRY2 leads to a local accumulation of F-actin (green) driving an increase in lateral tension and a reduction of cell height. (c) Apical and (d) basal top views and (e) lateral cross sections of a wing disk expressing RhoGEF2-CRY2 and CIBN::pmGFP, before and at the indicated times after a 2-min photoactivation. Cell membranes are labeled by Gap43::mCherry. Shown is the part of the wing disk that becomes optogenetically activated in the lateral region. Scale bar: 10 μm. (f) Boxplots of photoactivation-induced changes of cell height as well as apical and basal cross-section cell area ($N = 10$ wing disks). (g) Normalized basal tension before and at the indicated times after a 2-min photoactivation of RhoGEF2. Basal tension was normalized to the value before photoactivation [$N = 10$ wing disks, same wing disks as in panel (f)]. Significance was tested with a one-sample t-test (two-tailed) against the null hypothesis that the data come from a normal distribution with a mean equal to one ($^{*}p < 0.05$, $^{**}p < 0.01$, $^{***}p < 0.001$, n.s., not significant).

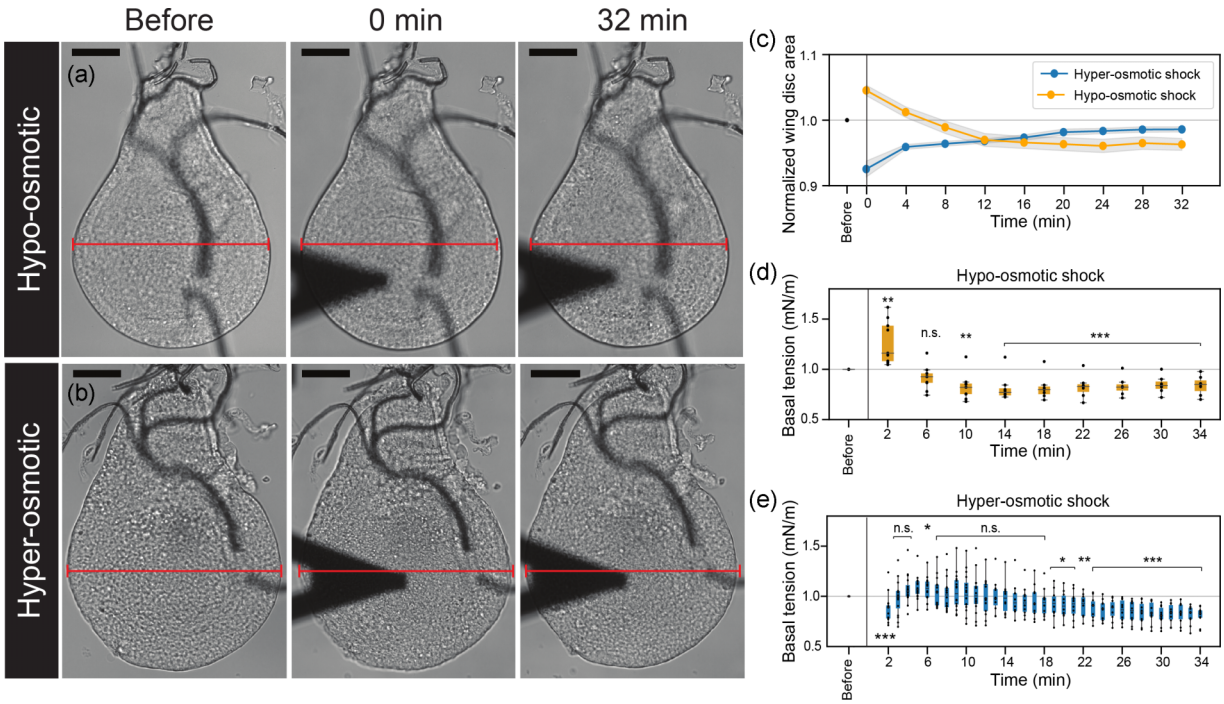

FIG. 5. Basal tension positively correlates with hydrostatic pressure. [(a), (b)] Brightfield time lapse images before and at the indicated times after (a) hypo-osmotic or (b) hyper-osmotic shock. Scale bar: 40 μm. The red line is of constant length and indicates changes in horizontal wing disk dimension with the left line edge coinciding with the left wing disk edge. (c) Normalized wing disk area before and at the indicated times after hypo-osmotic (orange) or hyper-osmotic (blue) shock ($N = 10$ wing disks). The areas were normalized by the value before the osmotic shock. Mean and s.e.m. are shown. [(d), (e)] Boxplots of basal tension before and at the indicated times after (d) hypo-osmotic or (e) hyper-osmotic shock. The tension was normalized by the value before the osmotic shock [$N = 10$, same wing disks as in panel (c)]. For panels (d) and (e), significance was tested with a one-sample t-test (two-tailed) against the null hypothesis that the data come from a normal distribution with a mean equal to one ($^{*}p < 0.05$, $^{**}p < 0.01$, $^{***}p < 0.001$, n.s., not significant).

an increase in actomyosin-based lateral tension leads to a temporary dilation of apical and basal cell surfaces with a corresponding increase in basal tension.

E. Osmotic shock changes basal area and basal tension

In order to test the response of basal tension to basal area changes with a second independent method, we decided to apply mild osmotic shocks to wing disks 72 h AEL. This treatment induces a temporary swelling (hypo-osmotic shock) or deswelling (hyper-osmotic shock) of the wing disk with a concomitant change of apical and basal cell areas. We note that osmotic shock is also connected to a temporary change of intracellular hydrostatic pressure [44]. In the following, we assume that the relative change of apical and basal cell areas corresponds to the relative change of overall wing disk area (see Materials and Methods).

To increase basal area, we first applied a hypo-osmotic shock to explanted wing disks by diluting the culture medium down by 25 % through addition of distilled water (see Materials and Methods). In response, wing disk area rapidly increased by $\varepsilon \approx 4.53 \pm 0.8\%$ (mean ± sem), on average, showing that the applied hypo-osmotic shock was efficient. Wing disk area subsequently relaxed to a value below the original area over a time span of ≈10 min [see Figs. 5(a) and 5(c)], perhaps through active volume regulation of the cells [45,46]. Concomitantly, we performed AFM measurements of basal tension. We found that right after application of the osmotic shock (measured ≈2 min after addition of distilled water), basal tension was increased by $\Delta\tilde{\sigma}_b \approx 27.24 \pm 7.23\%$ on average as compared to measurements before the shock. After this initial peak, basal tension relaxed to a value below the original tension corresponding to a reduced value of wing disk area at longer times [see Figs. 5(c) and 5(d)].

To decrease basal cell areas, we applied a hyper-osmotic shock to explanted wing disks by increasing the concentration of the culture medium through addition of sorbitol to a final concentration of 13 mM (see Materials and Methods). In response, wing disk mean area was decreasing by ≈7.46 ± 1.22% with a subsequent recovery to a slightly reduced value over a time span of ≈20 min [see Figs. 5(b) and 5(c)]. Accompanying AFM measurements showed an average reduction in basal tension by ≈17 ± 1.94% right after application of the hyper-osmotic shock (measured ≈2 min after addition of sorbitol). Over time, basal tension converges to a value which is reduced as compared to initial tension corresponding to reduced wing disk area at later times [see Figs. 5(c) and 5(e)]. Thus, as predicted from our model, changes in basal cell areas positively correlate with changes in basal tension (and wing disk area) during both hypo-osmotic and hyper-osmotic shock.

Based on the assumption that basal tension changes upon osmotic shock were mainly triggered through changes in elastic stretch of the basement membrane, we used our

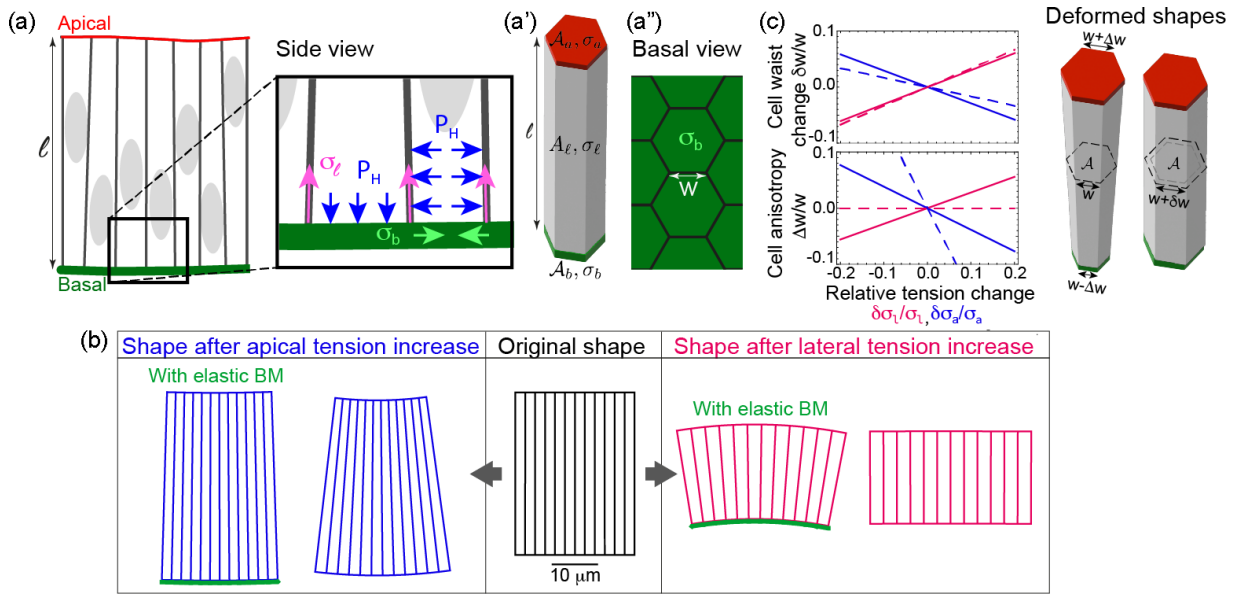

FIG. 6. A model for vertical and horizontal force balance of the wing disk epithelium taking into account lateral, apical, and basal tension as well as intracellular hydrostatic pressure. (a) Vertical force balance at the basal side is achieved through (i) hydrostatic pressure P_H pushing against the basal surface (blue vertical arrows) and (ii) the vertical component of contractile tension, σ_ℓ, in the lateral cell surfaces pulling on the basement surface (pink arrows on lateral cell interfaces). Horizontal force balance emerges through the interplay between (i) contractile apical and basal tension (σ_b, light green arrows) and (ii) hydrostatic pressure pushing against the lateral cell surfaces in the epithelium (blue horizontal arrows). In a weakly curved epithelium, vertical and horizontal force balances require that $P_H\mathcal{A} = \sigma_\ell\mathcal{P}$ and that $P_H A_l = 2(\sigma_b + \sigma_a)\mathcal{P}$, where A_l, $\mathcal{P}$, and $\mathcal{A}$ denote lateral cell surface area, the perimeter of the cellular cross section, and the midplane cross-section area, respectively [see Eqs. (2) and (3)]. (a′) Schematic of a model cell in three dimensions. (a″) Basal view on the epithelium illustrating cellular cross sections. (b) An elastic basement membrane (BM) changes cell shape regulation qualitatively. An initially top-down-symmetric columnar epithelium (see black schematic in the center) changes its shape upon modulations of (i) apical tension (blue schematics on the left) or (ii) lateral tension (red schematics on the right). The curvature that emerges in this process depends qualitatively on the presence of an elastic BM. Upon apical tension changes, emerging curvature is diminished through an elastic BM while upon lateral tension changes the tissue only becomes curved in the presence of an elastic BM. Parameter choices for the original shape (center, black) were chosen according to our measurements in the wing disk epithelium: $\sigma_a = \sigma_b = 0.3$ mN/m, $\mathcal{A}_0 = 10\ \mu\text{m}^2$, $l = 35\ \mu$m. The edge length w was set to $\mathcal{A}_b = 1.2\mathcal{A}_0$ corresponding to a basal stretch of 20% in homeostasis. To obtain perturbed shapes, apical tension is increased by 25% (left-hand side, blue) and lateral tension is increased by 100% (right-hand side, red). For the elastic case, we assume $K_b = 1$ mN/m and $K_b = 0$ mN/m otherwise. (c) Quantification of relative changes of cellular waist $\delta w/w$ and cellular anisotropy $\Delta w/w$ in the presence (solid lines) or absence (dashed lines) of an elastic basement membrane triggered by changes of apical tension $\delta\sigma_a/\sigma_a$ or lateral tension $\delta\sigma_l/\sigma_l$ according to the model discussed in Supplemental Material Sec. 1 [20]. Parameters were as in panel (b).

experimental results to estimate the elastic modulus of the basement membrane, K_b. For hypo-osmotic shocks, median tension values before osmotic shock were $\sigma_b^{\text{bef}} = 0.44$ mN/m. Together with a relative tension increase of $\Delta\tilde{\sigma}_b \approx 27.24 \pm 7.23\%$ and a surface area increase of $\varepsilon \approx 4.53 \pm 0.8\%$ right after the shock, we can estimate $K_b \approx \Delta\tilde{\sigma}_b/\varepsilon \times \sigma_b^{\text{bef}} = 2.64 \pm 1.16$ mN/m using linear error propagation. For hyper-osmotic shocks, median basal tension values before osmotic shock were $\sigma_b^{\text{bef}} = 0.34$ mN/m. Together with a relative tension decrease of $\approx 17 \pm 1.94\%$ and a surface area decrease of $\approx 7.46 \pm 1.22\%$ right after the shock, we estimated $K_b \approx 0.77 \pm 0.22$ mN/m. We speculate that the larger elastic modulus for hypo-osmotic stretching might originate, at least partly, in the nonlinear strain stiffening of basement membranes as has been reported previously [47–50].

F. Active tension outside basal cell faces generates a force balance with basal elastic tension

Our experiments indicate that the basement membrane of the wing disk epithelium is subject to a dilational elastic stretch in epithelial homeostasis. However, elastic stretch needs to be maintained by forces to persist. We therefore asked, which forces in the cell can lead to the generation of this elastic stretch in epithelial homeostasis? To provide an explanation approach from a physics point of view, we discuss a model of cellular force balances that explains how active stresses outside of basal cell faces can induce basal elastic stretch. To this end, we consider an energy functional of epithelial cells taking into account the presence of an elastic basement membrane,

$$E_{\text{cell}} = \mathcal{A}_a\sigma_a + \mathcal{A}_b\sigma_b^{\text{act}} + \frac{K_b}{2}\frac{(\mathcal{A}_b - \mathcal{A}_0)^2}{\mathcal{A}_0} + A_l\sigma_l - P_H V_{\text{cell}}, \tag{1}$$

which is a simplified version of the vertex model energy functional [51] where V_{cell} and P_H denote cellular volume and cell-internal hydrostatic pressure P_H, respectively. Here, we include cell surface tensions for all cellular faces (apical, σ_a; basal, σ_b; lateral, σ_l) with associated apical and basal cross-section surface areas $\mathcal{A}_a$, $\mathcal{A}_b$ [see Fig. 6(a)]. Furthermore, A_l

denotes the total area spanned by lateral surfaces of one cell. We note that the area bulk modulus $K_b = Eh/2/(1-\nu)$ for an isotropic layer with Young's modulus E, Poisson ratio ν, and layer thickness h [52].

Following a common strategy in physics, we consider first the most reductionist simple scenario of a top-down-symmetric flat epithelium with equal apical and basal cell surfaces $\mathcal{A}_a = \mathcal{A}_b = \mathcal{A}$, and identical apical and basal cell surface tensions $\sigma_a = \sigma_b$. This epithelial conformation corresponds to our default measurement situation with wing disks before fold formation. By variation of the energy functional (1) with respect to $\mathcal{A}$ and ℓ, we obtain as conditions of minimal energy

$$0 = 2\sigma_b + \frac{\partial A_l}{\partial \mathcal{A}}\sigma_l - P_H\ell, \quad 0 = \sigma_l\mathcal{P} - P_H\mathcal{A}, \tag{2}$$

where we use that $V_{\text{cell}} = \mathcal{A}\ell$, $\sigma_b = K_b(\mathcal{A}_b - \mathcal{A}_0)/\mathcal{A}_0 + \sigma_b^{\text{act}}$, and that $A_l = \ell\mathcal{P}$ with $\mathcal{P}$ the perimeter of the apical and basal cell cross section. In particular, for a hexagonal apical and basal cell cross section with edge length w, we have $\mathcal{P} = 6w$ and $\mathcal{A} = 3\sqrt{3}w^2/2$ and thus $\partial A_l/\partial\mathcal{A} = 2\ell/(\sqrt{3}w)$ and we obtain with Eq. (2) the following proportionalities:

$$\sigma_b = \frac{\ell\sigma_\ell}{\sqrt{3}w}, \quad \sigma_b = \frac{P_H\ell}{4}, \tag{3}$$

illustrating the balance of active and passive stresses in an epithelial cell [see Fig. 6(a)]. In short, our model shows that actomyosin-induced active tensions in cellular faces away from the basal side, i.e., lateral and apical, can maintain an intracellular hydrostatic pressure excess and a passive elastic stretch of the solidlike structures at the basal cell face. We note that relationships (3) also hold to first order in weakly curved epithelia if σ_b is replaced by $(\sigma_a + \sigma_b)/2$ as can be inferred from Eqs. (S2) and (S3).

We further asked how basal tension changes when lateral cell tensions or hydrostatic pressure are modified in the epithelium. In the framework of our model, we find for small changes of hydrostatic pressure, δP_H, or lateral tension, $\delta\sigma_\ell$, that induced changes of basal tension are given to linear order by

$$\delta\sigma_b = \frac{\delta\sigma_\ell 4\ell w^2 K_b}{\left(3w_0^2\sigma_b + 2w^2K_b\right)\sqrt{3}w}, \quad \delta\sigma_b = \frac{\delta P_H \ell w^2 K_b}{2\left(w^2K_b - w_0^2\sigma_b\right)}, \tag{4}$$

for a flat top-down-symmetric epithelium with hexagonal cross section. Here, we assumed that $\delta\sigma_a = 0$ because σ_a is subject to active regulation. In addition, we assumed constant cell volume such that $\delta V_{\text{cell}} = 0 = \delta\ell\mathcal{A} + \ell(\partial\mathcal{A}/\partial w)\delta w$ and therefore $\delta\ell = -(\ell/\mathcal{A})(\partial\mathcal{A}/\partial w)\delta w$. Furthermore, we anticipated that basal tension changes due to elastic stretch with $\delta\sigma_b = K_b\delta\mathcal{A}/\mathcal{A}_0 = K_b\delta w/\mathcal{A}_0 \times \partial\mathcal{A}/\partial w$. (Note that, provided the basement membrane is under moderate elastic stretch before the perturbation, i.e., stretch smaller than 100%, we have that the denominator in the second relation of Eq. (4) $(w^2K_b - w_0^2\sigma_b) > 0$.) We conclude that, according to our model of force balances, changes in lateral surface tension, $\delta\sigma_\ell$, or changes in hydrostatic pressure, δP_H, in the cell are predicted to trigger proportional changes in basal tension, $\delta\sigma_b$ [see Eq. (4)]. This further explains our experimental findings presented in Figs. 4 and 5.

The presence of an elastic, tensed basement membrane changes epithelial morphogenesis qualitatively. This can be seen by an extension of the above model to weakly curved epithelia (see Supplemental Material Sec. 1 [20]). In particular, we can use this extended model to predict how epithelial curvature depends on tension changes with or without an elastic structure at the basal side. The presence of an elastic basement membrane introduces fundamental changes to how an initially top-down-symmetric epithelium responds to changes in apical and lateral tension; while curvature induction due to apical tension change is decreased, curvature induction upon lateral tension changes can only happen in the presence of an elastic basement membrane (see Figs. 6(b) and 6(c) and the Supplemental Material [20]). We infer that cell shape anisotropy only emerges upon lateral tension changes if an elastic component is present in the regulation of basal or apical cell surface tension. We note that this idea has been previously discussed in the literature, but without consideration of involved force balances [17].

III. DISCUSSION

In this study, we provided direct quantitative measurements of basal tension in the columnar epithelium of explanted wing disks from the third instar larva of the fruit fly *Drosophila melanogaster*. We used an established method of AFM indentation to determine basal cell surface tension by the scaled slope of force-indentation curves (see Fig. 1, Fig. S1, and Sec. IV G [23–25]). In particular, we find that basal tensions in wing disk epithelia are in the range 0.2–0.5 mN/m and therefore similar to tension values of the actin cortex of isolated interphase cells measured with diverse methods [27–30].

In the past, many studies have been dedicated to the mechanics of the basement membranes and its dominant contribution to overall tissue mechanics. However, such studies have been mostly assuming that the basement membrane responds to deformation like a tension-free, passive material [47,53–55]. Correspondingly, the possibility of a homeostatic elastic stretch and an associated basal tension contribution has been disregarded. Few previous estimates of basal tension in epithelia have been reported, but without a detailed analysis of the basement membrane contribution; micropipette aspiration experiments on mouse blastocysts and 8-cell stage mouse embryos provided similar basal tension estimates in the ranges 0.5–1 mN/m and 0.2–0.5 mN/m, respectively [56,57]. By contrast, Yang *et al.* determined basal tensions in intestinal organoids by micropipette aspiration, finding considerably higher values in the range 3–6 mN/m [58]. Taken together, these results suggest that basal tension in epithelia may vary by at least one order of magnitude, perhaps in dependence of hydrostatic pressure in the lumen.

Perturbing wing disks pharmacologically, we find that both basement membrane and actomyosin contribute to basal tension generation [see Figs. 1(d)–1(h)]. In accordance with our study, Yang *et al.* and Maitre *et al.* found evidence that actomyosin contributes to basal tension generation [57,58]. Furthermore, ablation experiments on cell edges of lateral cell faces previously showed that edge tension proximal to the basal side is reduced by basement membrane degradation through incubation with collagenase or localized MMP2 expression [15].

In order to understand how the basement membrane contributes to basal tension, we investigated the turnover dynamics of the basement membrane to infer whether it can store elastic stresses on the timescale of fold formation. Performing imaging of collagen IV in the basement membrane for several hours, we observed that turnover and mobility of collagen IV is slow (≈30 h), suggesting a solidlike nature of the basement membrane on timescales of several hours (see Fig. 3). This observation of slow basement membrane turnover is in accordance with the majority of earlier reports about the material properties of basement membranes [59]. The basement membrane turnover in *Drosophila* embryos was, however, measured to be slightly faster (7–10 h) [60].

Given that the basement membrane has solidlike properties, we infer that the basement membrane can be stretched elastically and can store elastic stresses on long timescales, thereby contributing to basal tension. Importantly, our model of cellular force balance predicts that the presence of an elastic layer at the basal side introduces fundamental differences to how cell shape responds to tension changes, in particular enabling changes in lateral tension to induce epithelial curvature [see Fig. 6(b)]. The presence of elastic stretch in the basement membrane of the wing disk epithelium has also been reported by Harmansa *et al.*, who linked ECM-associated elastic stretch to epithelial thickening and doming in the wing disk [16]. Furthermore, Nematbakhsh *et al.* proposed an elastic solidlike nature of the ECM as a means to conserve epithelial organ shape after actomyosin-driven tissue bending [17]. However, neither of these two studies provided measurements of basal tension.

Passive elastic stretch and corresponding elastic stresses in the basement membrane need to be maintained by active cellular driving forces. As potential candidates, we identified (i) actomyosin-dependent contractility in lateral cell faces using localized optogenetic actomyosin activation and (ii) intracellular hydrostatic pressure employing osmotic shocks (see Figs. 4 and 5). We note that the scenario of an elastic basement membrane stretch balanced by an active expansile cell layer is further supported by our observation of basal cell area widening upon collagenase-induced basement membrane degradation [see Fig. 1(i)]. In addition, basal area shrinkage upon treatment with the Rock inhibitor Y27632 and Latrunculin A [see Figs. 1(j) and 1(k)] supports that basement membrane stretch is maintained by actomyosin forces. From measurements of basal tension changes during induced wing disk area changes, we could infer estimates of the basal elastic modulus in the range 0.5–3 mN/m. Using previously reported thickness estimates of 0.1 μm of the wing basement membrane in the third instar larva [61], we can associate a basement membrane Young's modulus of ≈5–30 kPa assuming a Poisson ratio of 0.5 [62,63]. This estimate is in the lower range of previously measured elastic moduli of basement membranes, which were reported to lie between 1 and 1000 kPa [64].

In summary, the key finding of this study is the disclosure of a new mechanism of basal tension regulation in epithelia; tension is built up through elastic stretch of the solidlike basement membrane. This stretch is generated by actomyosin contractility outside of basal cell faces. This finding reveals that basal tension generation has quite distinct properties from actomyosin-based apical tension generation. We propose that the asymmetry in apical and basal tension regulation constitutes an important tool of morphogenesis to induce asymmetries in apical and basal tension as well as curvature in the epithelium.

TABLE I. *Drosophila melanogaster* fly stocks.

Fly stocks	Source	Ref.
indy-GFP (YC0017)		[65]
viking-GFP		[39]
30A-GAL4	Bloomington *Drosophila* stock center	RRID: BDSC_37534
UAS-CD8-mCherry/CyO		[66]
UASp-CIBN::pmGFP	Gift from Stefano De Renzis, EMBL, Heidelberg, Germany	[67]
ap-Gal4	Gift from Elisabeth Knust	
tub-Gal80^{ts}		[68]
UAS-sqh-Gap43::mCherry		[69]
sqh-GFP		[70]

IV. MATERIALS AND METHODS

A. Fly stocks and genetics

Flies were raised on standard fly food and maintained at 25 °C unless stated otherwise. Table I lists the *Drosophila melanogaster* fly stocks that were used.

Standard fly husbandry and genetic methodologies were used to cross *Drosophila* strains. The detailed genotypes for each experiment are listed in Table II.

B. Time-lapse live imaging and FRAP experiments

Staging, dissection, and culture of 72 h AEL wing disks were done as described previously [15]. Imaging as reported in Fig. 3 was performed using a Zeiss LSM700 confocal microscope, using a 40×/1.25 numerical aperture water immersion objective. Image stacks of 30 slices were taken such that the total height of the wing disk was covered (≈40 μm). The pinhole aperture was chosen such that the optical section thickness was equal to the distance between neighboring

TABLE II. Detailed genotypes for each experiment.

Figure(s)	Genotype
1(b)–1(h)	*y w;vkg-GFP,30A-GAL4, UAS-CD8-mCherry/CyO*
1(i)–1(k)	*indy-GFP*
2(b)	*y w;vkg-GFP,30A-GAL4, UAS-CD8-mCherry/CyO*
2(c)–2(f)	*indy-GFP;30A-GAL4, UAS-CD8-mCherry/CyO*
3(a)–3(i)	y w;*vkg-GFP*
4(a)–4(g)	*ap-Gal4, tub-Gal80ts, UASp-CIBN::pmGFP; UASp-RhoGEF2-CRY2/sqh-Gap43::mCherry*
5(a)–5(e)	*y w;vkg-GFP,30A-GAL4, UAS-CD8-mCherry/CyO*
S1(a)–S1(e)	*y w;vkg-GFP,30A-GAL4, UAS-CD8-cherry/CyO*
S2(a)–S2(c)	*y w;vkg-GFP,30A-GAL4, UAS-CD8-mCherry/CyO*
S2(d)–S2(f)	*sqh-GFP*
S2(g)–S2(i)	*indy-GFP*
S4(a)–S4(f)	*y w;vkg-GFP,30A-GAL4, UAS-CD8-mCherry/CyO*
S5(a)–S5(l)	*indy-GFP*

slices. Wing disks were mounted with their basal side towards the objective. We chose 512×512 pixels per image and recorded with 2% laser power.

To observe collagen IV dynamics long term [Figs. 3(a)–3(e)], we carried out the following imaging protocol. First, an initial Z stack of the whole tissue was acquired. Then, two square-shaped regions of interest (30×30 μm^2) were chosen, one in the hinge/notum region and another one in the pouch. Subsequently, we imaged a time series of 42 frames of both regions with a time interval of 10 min for a total time of ≈7 h. In the end, a final Z stack of the whole wing disk was acquired.

Fluorescence recovery after photobleaching (FRAP) experiments as described in Figs. 3(f)–3(i) were performed in a similar manner. First, an initial Z stack of the full wing disk was recorded. Then, photobleaching was performed on a square region (30×30 μm^2) with a 488 nm laser at 100% power for 28 s, giving approximately 90% fluorescence intensity reduction. Subsequently, a time series of 42 Z stacks of a 45×45 μm^2 square region (bleached region with surroundings) was recorded with a time interval of 10 min. In the end, a final Z stack of the full wing disk was acquired. All image analysis was performed using FIJI [71] as described for the confocal imaging. All measurements were performed at room temperature.

For long-term imaging both with and without photobleaching, we performed image analysis using FIJI [71] to measure the mean of the summed stack intensities of square regions of interest over time [Figs. 3(d) and 3(h)]. Fluorescence intensities were normalized by the fluorescence intensity value at the first time point.

To quantify the influence of bleaching introduced through long-term imaging [Figs. 3(a)–3(e)], the ratio of initial and final mean fluorescence intensity was determined for both square regions and compared to an analogous fluorescence intensity ratio for a square region of equal size outside of the long-term imaged square regions [Fig. 3(c)]. This region is labeled as "OR" and depicted with a cyan frame [see Figs. 3(a) and 3(c)].

For the fluorescence line profile in Fig. 3(i), we chose a line thickness of approximately one-third of the bleaching frame height.

C. Acquisition and analysis of AFM force-indentation curves

Wing disk indentations were performed using an atomic force microscope (Nanowizard I, JPK Instruments) mounted on a Zeiss Axiovert 200M wide-field microscope, 20× objective (Zeiss, Plan Apochromat, numerical aperture (NA) = 0.8) along with a charge-coupled device (CCD) camera (DMK 23U445 from Theimagingsource).

During measurements, dissected wing disks were placed into cell culture dishes (fluorodish FD35-100) coated with poly-D-lysine. The coating was performed by adding 2 ml of poly-D-lysine solution (0.1 mg/ml in PBS, Gibco A3890401) to the dishes and incubating overnight at 4 °C. Then, the poly-D-lysine solution was removed and dishes were rinsed once with distilled water. Afterwards, we dried the plates with a compressed air gun. Plates were stored at 4 °C for up to 5 days.

AFM cantilevers with pyramidal tips were used in all experiments with a nominal spring constant of 0.01 N/m (MLCT-C, Bruker AFM probes, opening angle 17.5°, curvature radius 20 nm). Preceding each experiment, the actual cantilever spring constant was measured by means of thermal noise analysis (built-in software, JPK). Actual spring constant values ranged from 0.01 to 0.02 N/m. All measurements were performed in 3 ml of Grace's culture medium at room temperature. AFM measurements were carried out in contact mode. For tension measurements presented in Figs. 1, 2(b), and 5(d), a measurement consisted of 64 force-indentation curves acquired on a regular square lattice of 8×8 points with an edge length of 10 μm. For tension measurements presented in Figs. 4(g) and 5(e), a measurement consisted of 16 force-indentation curves acquired on a regular square lattice of 4×4 points with an edge length of 10 μm.

For all grid configurations, indentations were carried out continuously such that the cantilever was indenting one grid point after another. After the completion of the full grid, the indentation protocol started over. Indentations were performed at an extension speed of 1 μm/s up to a maximal force of 500 pN. This force maximum was typically achieved at an indentation of 0.5–1.5 μm. The position of the grid was targeted by eye in the center of the wing pouch unless stated otherwise.

For position-dependent measurements shown in Figs. 2(c)–2(j), force indentations were performed on a rectangular grid with 8×14 grid points spanning an area of 40×70 μm^2 (68 h AEL) or 6×20 grid points spanning an area of 30×100 μm^2 (72 h AEL).

In order to get the slope of the force-indentation curves, we used the JPK Data Processing software. First we applied a baseline subtraction, including the correction for the offset plus tilt of the curves. This was followed by a subtraction of the x offset (contact point) and a correction for the bending of the cantilever (vertical tip position). Afterwards, we performed a linear fit in the range between the contact point and 500 pN. The data processing and plotting were performed using PYTHON.

The median of the successfully fitted approximately 64 curves represents the basal tension of one sample and corresponds to one data point in boxplots in Figs. 1(d)–1(h), 2(b), 4(g), 5(d), and 5(e), and Supplemental Material Figs. S1(c)–S1(e) and S2(a)–S2(c) [20].

For tension values on an X-Y grid as reported in Figs. 2(d) and 2(h), indentations were performed three times per grid point in every wing disk. The tension value of each grid point is the average of three indentation measurements. To generate the curves in Figs. 2(e) and 2(i), we calculated the median of tension values measured along the Y axis for a fixed X position for each wing disk. Tensions were then normalized by the tension value in the center of the hinge region ($X = 0$). Finally, normalized basal tension values were averaged over several wing disks and plotted across the X position (number of wing disks averaged: $N = 7$ for the 68 h AEL and $N = 11$ for the 72 h AEL wing disk).

D. Wing disk drug treatment and AFM measurements

Ex vivo drug treatment was applied to wing disks explanted 72 h AEL. For that purpose, wing disks were transferred to a coated glass bottom dish and immersed in 3 ml culture

medium as explained in Sec. IV C. Then, an initial measurement series of AFM indentations along an 8×8 grid was performed in the center of the pouch region. Afterwards, the AFM head was unmounted and the respective drug was added to the medium. To ensure proper mixing, pipette pumping was performed. Afterwards, the AFM head was mounted again as quickly as possible (∼2 min) and AFM indentations along an 8×8 grid were continuously carried out for approximately 30 min (see Figs. 1(d)–1(h) and Supplemental Material Figs. S2(a)–S2(c) [20]). AFM force-indentation curves were analyzed to obtain basal tension estimates as described in Sec. IV C. The time evolutions of basal tensions after drug addition are shown in Supplemental Material Figs. S2(a)–S2(c) [20]. For all drug treatments, we concluded that the full effect on wing disk mechanics was present at the latest after 15 min of treatment time.

The following drug concentrations were used: 1 mM Y-27632 (Biomol AG-CR1-3564-M010, 25 mM stock in PBS), 0.2% collagenase type I (Sigma-Aldrich SCR103, 1% stock in PBS), 4 μM Latrunculin A (Biomol AG-CN2-0027-C100, 1 mM stock in DMSO). In control measurements, AFM indentations were performed before and after incubation in PBS (4%) and with DMSO at a final concentration of 0.1% in the culture medium [see Figs. 1(g) and 1(h)].

For measuring the change in apical and basal area after drug treatment, cell membranes in the pouch region were visualized by Indy-GFP. Wing disks were mounted with their apical side tethered to the glass bottom dish. Imaging was performed using a Leica SP8 MP confocal microscope. Image analysis of drug treatment was done using FIJI [71]. In order to be able to visualize the basal surface of the cells, the signal-to-noise ratio was improved using a machine-learning image restoration plug-in (Content-Aware Image restoration, CARE [72]). The apical plane was identified by the accumulation of signal intensity. The basal plane was identified by focusing the image plane on the basal surface of cells. Cell cross sections were then segmented and tracked over time using Tissue Analyzer [73]. As not all cells could be segmented over the entire time course of the experiment, we identified groups of cells (five or six cells per group) which could be successfully segmented and tracked over time [73]. The area of the group was measured using Tissue Analyzer [73] or FIJI [71]. For each wing disk, five groups were analyzed and the group-averaged area change was determined.

To quantify myosin levels at the basal surface of the cells, myosin activity was visualized by Sqh-GFP. Imaging was performed using an upright Leica Stellaris 8 confocal microscope. Wing disks were mounted with their apical side tethered to the glass bottom dish. Image Z stacks were taken from basal to apical every 2 min. Myosin intensity was measured on a squared region (30×30 μm^2) using FIJI [71]. The peak of the mean fluorescence intensity Z profile was used to identify the basal surface.

E. Optogenetics experiments and analysis

Incubation, dissection, and culture of wing disks were done as described previously [15,43]. Larvae were incubated in the dark at 25 °C and transferred to 29 °C 3 days before dissection. Wing disks were placed into cell culture dishes (fluorodish FD35-100) coated with poly-D-lysine. Two-photon activation and imaging were performed via a Zeiss LSM 980 confocal laser scanning microscope, using a C-Apochromat 40×/1.2 water objective.

For every wing disk measurement, the following protocol was carried out. First, wing disks were mounted with the apical side facing the objective. A region of interest of 50 × 30 μm^2 was defined in the central pouch region of wing disks. Before photoactivation and AFM measurements, an initial Z stack in the mCherry channel (561 nm) was acquired (45 planes, 1 μm spacing). Two-photon photoactivation was performed with light of 950 nm wavelength at 8% laser power with bidirectional scanning. A 15-μm-thick Z interval in the center of the wing disk epithelium was photoactivated for 2 min by scanning 15 planes 1 μm apart. After photoactivation, a Z stack (45 planes, 1 μm spacing) of the region of interest was recorded in the mCherry channel in a time series (five frames, 2-min interval). After verifying the effectiveness of the optogenetic activation by imaging, an initial AFM measurement was acquired on a regular square lattice of 4×4 on the tissue (see Sec. IV C above). Afterwards, a second 2-min lateral photoactivation was carried out, immediately followed by continuous AFM indentations on a 4×4 grid for 10 min (without confocal imaging).

Image analysis of optogenetic experiments was carried out in FIJI [71]. To quantify cell height in the wing disk epithelium, a vertical cross section was acquired using the reslice tool on a middle section of the imaged region. In the cross section, we acquired the fluorescence intensity profile on a line (≈30 μm width) encompassing the full Z range. We subtracted the background fluorescence intensity and quantified tissue height as the length of the line interval where the fluorescence intensity was reduced by no less than 20% as compared to the maximal fluorescence intensity value.

Apical cell areas were determined by choosing a plane between the first 5 to 10 slices. Afterwards, we measured the area of a set of cells (four or five) whose apical region stayed focused in the same plane before and after photoactivation. The procedure for measuring basal cell areas was similar to apical cell areas. The plane was chosen between the last 5 to 10 slices of the Z stack.

F. Osmotic shocks

Osmotic shock experiments in conjunction with AFM measurements were carried out analogous to AFM measurements before and after reagent treatment as described in Sec. IV D. Instead of reagent additions, 1 ml of dH_20 was added to 3 ml of medium in the dish to reduce the medium osmolarity to 75% for hypo-osmotic shock experiments. For hyper-osmotic shock experiments, sorbitol (Sigma S1000000) solution was added to a final concentration of 13 mM to the medium. The overall wing disk area was determined by drawing the outline of transmitted light images using the polygon selection tool in FIJI [71].

G. Using AFM indentation for basal tension measurements: A guide

To our best knowledge, our study is the first that uses AFM indentation for the determination of mechanical tension in

basement membranes. Therefore, we provide a thorough discussion of the justification of its applicability, analysis steps, and sources of error in this section.

We analyzed obtained AFM force-indentation data by applying the mechanical model of indentation into a thin, flat, tensed elastic sheet which we identify with the composite layer constituted by the basement membrane and the actin cortex at the basal side of the columnar epithelium. This analysis choice was based on (i) the observation that the thin basement membrane sheet dominates the force response of AFM indentation [see Supplemental Material Fig. S1(a)], (ii) observations that the basement membrane is under contractile tension (see Figs. 1(i)–1(k) and Ref. [15]), as well as (iii) the theoretical considerations in the two sections below ("Indentation of a tensed elastic sheet" and "The Hertz model").

Theoretical studies predict $F = \pi\sigma_b\delta$ for indentation into a thin tensed sheet, where F is the force, δ is the cantilever indentation, and σ_b is the tension due to elastic membrane stretch [74,75]. Correspondingly, we estimate basal tension in the wing disk as $\sigma_b = F'_{\mathrm{lin}}/\pi$ throughout this paper, where F'_{lin} is the fitted linear slope of the measured force-indentation curve [see Fig. 1(c)]. We note that this analysis scheme has been previously used to determine actin cortical tension in single cells and epithelial sheets [24,25]. Furthermore, this method is also commonly used to determine the tension in the cell walls of pressurized plant cells (see, e.g., Ref. [23]). We note that this modeling approach requires indentation larger than the thickness of the basement membrane layer. In our assay, typical indentation depths were 0.5 μm or larger which fulfils this condition as it is larger than previous thickness estimates of 0.1 μm of the basement membrane for young third instar larvae [61].

Error estimates. Using theory (see Supplemental Material, Sec. 2 [20]), we estimate that the influence of nonvanishing basement membrane thickness tends to yield underestimated basal tension estimates with an error of up to 15%. Furthermore, since in the case of collagenase-digested basement membranes the cytoplasmic bulk starts to dominate the mechanical response, basal tension estimates obtained from linear force fits in this situation are "apparent tensions" that quantify the magnitude of force increase upon indentation and that represent an upper bound of actual basal tension.

Indentation of a tensed elastic sheet. Theoretical studies predict a force increase of the form $F = \pi\sigma_{\mathrm{pre}}\delta + K_b C\delta^3$ for indentation into a tensed, disk-shaped elastic sheet which is clamped at the periphery [74,75]. (Here, σ_{pre} is the preexisting tension, C is a material constant that depends on the Poisson ratio and the disk diameter, and K_b is the elastic modulus of the sheet.) For small indentations δ, the theory thus predicts that $F \propto \delta$ if the tension $\sigma_{\mathrm{pre}} \neq 0$. (A similar result has been found for indentation into pressurized elastic shells with preexisting in-plane tension [76].) To find out if our data support the existence of a nonvanishing tension value, we fit power laws of varying exponent to measured force-indentation curves. We find on average an exponent of ≈1.35 (see Supplemental Material Fig. S1 and the next section). Since the exponent 1.35 is close to 1, we concluded that the mechanical model of indentation into a tensed elastic sheet is an appropriate model for our measurements.

The observed exponent likely exceeds 1 because of two reasons: (i) we overestimate power-law exponents of perfectly linear force increases due to data smoothing as part of the analysis process [see Supplemental Material Fig. S6(d), S6(e)], and (ii) our model for data analysis does not take into account that we are indenting a sheet with a nonvanishing thickness. The model assumes a simplified scenario of indentation into a two-dimensional sheet without any extension normal to the plane of the sheet. In the presence of a nonvanishing sheet thickness, there is an additional force contribution that stems from the local indenter penetration into the sheet. This phenomenon gives rise to a force increase that is $\propto\delta^2$ at the beginning of the force-indentation curve (for a pyramidal indenter). For greater indentations, the force-indentation curve then transitions to a linear regime [see Supplemental Material Fig. S6(d)]. Since our analysis of power-law fitting provides only one power-law readout for the entire force-indentation curve up to the peak force, we thereby increase the fitted power-law exponent of the force-indentation curve (see Supplemental Material Fig. S6 and Ref. [23]). A more detailed discussion of how indenter penetration changes fitted power laws is given in the Supplemental Material, Sec. 2 [20].

The Hertz model. The most common model for the analysis of AFM indentation is the Hertz model which assumes that the force response stems from indentation into an elastic half space [77]. It predicts a parabolic increase of the force $F \propto \delta^2$ corresponding to a power law with exponent 2 for a pyramidal indenter [24,25,77]. Here, we ruled out the appropriateness of the Hertz model for AFM indentation analysis given our experimental results that the (thin) basement membrane makes a substantial contribution to the mechanical response during AFM indentation [see Fig. 1(d)], in conjunction with our observation of the approximately linear force-indentation curves. Interestingly, upon treatment with collagenase, which disintegrates the basement membrane, we see not only a significant softening of the wing disk over time [see Supplemental Material Fig. S2(a)], but also an increase of the power-law exponent to a value of ≈2 (see Supplemental Material Figs. S1(b) and S1(c) [20]). This value matches closely the power law predicted for indentation into an elastic half space. This observation suggests that, only after basement membrane removal, the cytoplasmic bulk acts as the dominant mechanical element in AFM indentation.

Indentation speed choice. When establishing our experimental protocol, we verified that basal tension estimates of wing disks are not affected by slowing down indentation speed as compared to our standard speed choice of 1 μm/s [see Supplemental Material Figs. S4(a)–S4(d)]. We note that this is an important control experiment to verify the applicability of the method in the system under consideration; larger indentation speeds will inevitably increase the influence of viscous components such as the cytoplasm and the surrounding medium in the measured forces as their elastic modulus contribution scales with $2\pi f\eta$, where f is the frequency and η is the viscosity (see, e.g., Refs. [78,79]). Therefore, our chosen indentation speed of 1 μm/s represents a compromise between overall measurement speed (that is required to map the dynamics of tension after perturbations) and the avoidance of large viscous effects.

We note that we observed a hysteresis between indentation and retraction of AFM-measured force-indentation curves which was hardly changed also for slowed AFM speeds [see Supplemental Material Figs. S4(a)–S4(c) and S4(e)]. This observation indicates the presence of partial viscous dissipation during AFM indentation into the basement membrane layer due to friction [see Supplemental Material Figs. S4(e), S4(f), and S6(b)]. We note that this observation agrees qualitatively with predictions of a viscoelastic standard linear solid model, i.e., a model with a long-term elasticity of the material [80].

H. Power-law fitting of force-indentation curves

The MATLAB code for power-law fitting of force-indentation curves can found in Ref. [81] (script: FitAndAverageForceCurves.m). In short, force curves corresponding to the measurements on one wing disk at a specific time point are read in by the program and an average force-indentation curve is calculated. By least-squares fitting, the contact point of the averaged force-indentation curve is readjusted such that the curve is best captured by a linear increase in the log-log representation of the data (i.e., by a power law). Then, a second least-squares fit is performed to determine the optimal power-law exponent. For untreated wing disks (dissected 72 h AEL), the power-law exponent is typically between 1.2 and 1.4 (see Supplemental Material Fig. S1 [20]) and therefore closer to 1 than to 2. Using simulated force-indentation curves (see also Supplemental Material, Sec. 2 [20]), we estimate the error of this exponent fitting to be ≈ 0.15 due to imperfect localization of the contact point as well as due to noise and data smoothing.

ACKNOWLEDGMENTS

We thank Frank Jülicher and Carsten Werner for fruitful discussions on the topic. Furthermore, we thank Marko Brankatschk for giving generous access to his dissection microscopes and fly incubators. K.Y.G.S., C.D., and E.F.F. acknowledge financial support from the Deutsche Forschungsgemeinschaft under Germany's Excellence Strategy, EXC-2068-390729961, Cluster of Excellence Physics of Life of TU Dresden. Furthermore, E.F.F. was funded by the Deutsche Forschungsgemeinschaft (DFG, German Research Foundation), Project No. 495224622 (FI 2260/8-1) and FI 2260/9-1. In addition, the authors thank the CMCB Light Microscopy Facility and the PoL Light Microscopy Facility for excellent support.

K.Y.G.S., C.D., and E.F.F. conceived and designed the study. K.Y.G.S. performed the experiments and quantified the data. All authors discussed the data. K.Y.G.S., C.D., and E.F.F. wrote the manuscript.

The authors declare no competing interests.

[1] B. Alberts, A. Johnson, J. Lewis, M. Raff, K. Roberts, and P. Walter, *Molecular Biology of the Cell*, 4th ed. (Garland Science, New York, 2002).

[2] C. Guillot and T. Lecuit, Mechanics of epithelial tissue homeostasis and morphogenesis, Science **340**, 1185 (2013).

[3] U. Töpfer, K. Y. Guerra Santillán, E. Fischer-Friedrich, and C. Dahmann, Distinct contributions of ECM proteins to basement membrane mechanical properties in *Drosophila*, Development **149**, dev200456 (2022).

[4] J. Crest, A. Diz-Muñoz, D.-Y. Chen, D. A. Fletcher, and D. Bilder, Organ sculpting by patterned extracellular matrix stiffness, eLife **6**, e24958 (2017).

[5] J. Chlasta, P. Milani, G. Runel, J. L. Duteyrat, L. Arias, L. A. Lamiré, A. Boudaoud, and M. Grammont, Variations in basement membrane mechanics are linked to epithelial morphogenesis, Development **144**, 4350 (2017).

[6] R. Mollard and M. Dziadek, A correlation between epithelial proliferation rates, basement membrane component localization patterns, and morphogenetic potential in the embryonic mouse lung, Am. J. Respir. Cell Mol. Biol. **19**, 71 (1998).

[7] M. S. Brown, B. Abdollahi, O. M. Wilkins, H. Lu, P. Chakraborty, N. B. Ognjenovic, K. E. Muller, M. K. Jolly, B. C. Christensen, S. Hassanpour *et al.*, Phenotypic heterogeneity driven by plasticity of the intermediate EMT state governs disease progression and metastasis in breast cancer, Sci. Adv. **8**, eabj8002 (2022).

[8] D.-Y. Chen, J. Crest, S. J. Streichan, and D. Bilder, Extracellular matrix stiffness cues junctional remodeling for 3D tissue elongation, Nat. Commun. **10**, 3339 (2019).

[9] M. Tozluoğlu and Y. Mao, On folding morphogenesis, a mechanical problem, Philos. Trans. R. Soc. B **375**, 20190564 (2020).

[10] N. C. Heer and A. C. Martin, Tension, contraction and tissue morphogenesis, Development **144**, 4249 (2017).

[11] M. A. Morrissey and D. R. Sherwood, An active role for basement membrane assembly and modification in tissue sculpting, J. Cell Sci. **128**, 1661 (2015).

[12] J. V. Beira and R. Paro, The legacy of *Drosophila* imaginal discs, Chromosoma **125**, 573 (2016).

[13] J. C. Pastor-Pareja and T. Xu, Shaping cells and organs in *Drosophila* by opposing roles of fat body-secreted collagen IV and Perlecan, Dev. Cell **21**, 245 (2011).

[14] M. Ma, X. Cao, J. Dai, and J. C. Pastor-Pareja, Basement membrane manipulation in *Drosophila* wing discs affects Dpp retention but not growth mechanoregulation, Dev. Cell **42**, 97 (2017).

[15] L. Sui, S. Alt, M. Weigert, N. Dye, S. Eaton, F. Jug, E. W. Myers, F. Jülicher, G. Salbreux, and C. Dahmann, Differential lateral and basal tension drive folding of *Drosophila* wing discs through two distinct mechanisms, Nat. Commun. **9**, 4620 (2018).

[16] S. Harmansa, A. Erlich, C. Eloy, G. Zurlo, and T. Lecuit, Growth anisotropy of the extracellular matrix shapes a developing organ, Nat. Commun. **14**, 1220 (2023).

[17] A. Nematbakhsh, M. Levis, N. Kumar, W. Chen, J. J. Zartman, and M. Alber, Epithelial organ shape is generated by patterned actomyosin contractility and maintained by the extracellular matrix, PLoS Comput. Biol. **16**, e1008105 (2020).

[18] R. Etournay, M. Popović, M. Merkel, A. Nandi, C. Blasse, B. Aigouy, H. Brandl, G. Myers, G. Salbreux, F. Jülicher, and S. Eaton, Interplay of cell dynamics and epithelial tension during morphogenesis of the *Drosophila* pupal wing, eLife **4**, e07090 (2015).

[19] Y. Mao, A. L. Tournier, A. Hoppe, L. Kester, B. J. Thompson, and N. Tapon, Differential proliferation rates generate patterns of mechanical tension that orient tissue growth, EMBO J. **32**, 2790 (2013).

[20] See Supplemental Material at http://link.aps.org/supplemental/10.1103/PRXLife.2.013004 for power laws of force-indentation curves during reagent incubation (Fig. S1, supplement to Fig. 1, main text); for time evolution of basal tension, myosin intensity, and cell areas during reagent incubation (Fig. S2, supplement to Fig. 1, main text); the model of cellular force balance in weakly curved epithelia; force-indentation curves at diverse indentation speeds (Fig. S4); images of area changes of cells before and after reagent incubation (Fig. S5, supplement to Fig. 1, main text); and theory of AFM indentation. The Supplemental Material also contains Refs. [21,22].

[21] M. J. Rosenbluth, W. A. Lam, and D. A. Fletcher, Force microscopy of nonadherent cells: A comparison of leukemia cell deformability, Biophys. J. **90**, 2994 (2006).

[22] K. L. Johnson, *Contact Mechanics* (Cambridge University Press, Cambridge, UK, 1987).

[23] S. Tsugawa, Y. Yamasaki, S. Horiguchi, T. Zhang, T. Muto, Y. Nakaso, K. Ito, R. Takebayashi, K. Okano, E. Akita, R. Yasukuni, T. Demura, T. Mimura, K. Kawaguchi, and Y. Hosokawa, Elastic shell theory for plant cell wall stiffness reveals contributions of cell wall elasticity and turgor pressure in AFM measurement, Sci. Rep. **12**, 13044 (2022).

[24] S. Sen, S. Subramanian, and D. E. Discher, Indentation and adhesive probing of a cell membrane with AFM: Theoretical model and experiments, Biophys. J. **89**, 3203 (2005).

[25] A. Pietuch, B. R. Brückner, and A. Janshoff, Membrane tension homeostasis of epithelial cells through surface area regulation in response to osmotic stress, Biochim. Biophys. Acta: Mol. Cell Biol. **1833**, 712 (2013).

[26] L. Beauzamy, J. Derr, and A. Boudaoud, Quantifying hydrostatic pressure in plant cells by using indentation with an atomic force microscope, Biophys. J. **108**, 2448 (2015).

[27] E. Fischer-Friedrich, A. A. Hyman, F. Jülicher, D. J. Müller, and J. Helenius, Quantification of surface tension and internal pressure generated by single mitotic cells, Sci. Rep. **4**, 6213 (2014).

[28] J.-Y. Tinevez, U. Schulze, G. Salbreux, J. Roensch, J.-F. Joanny, and E. Paluch, Role of cortical tension in bleb growth, Proc. Natl. Acad. Sci. USA **106**, 18581 (2009).

[29] G. Salbreux, G. Charras, and E. Paluch, Actin cortex mechanics and cellular morphogenesis, Trend. Cell Biol. **22**, 536 (2012).

[30] K. Hosseini, A. Frenzel, and E. Fischer-Friedrich, EMT changes actin cortex rheology in a cell-cycle-dependent manner, Biophys. J. **120**, 3516 (2021).

[31] N. C. Heer, P. W. Miller, S. Chanet, N. Stoop, J. Dunkel, and A. C. Martin, Actomyosin-based tissue folding requires a multicellular myosin gradient, Development **144**, 1876 (2017).

[32] S. F. G. Krens, J. H. Veldhuis, V. Barone, D. Čapek, J.-L. Maître, G. W. Brodland, and C.-P. Heisenberg, Interstitial fluid osmolarity modulates the action of differential tissue surface tension in progenitor cell segregation during gastrulation, Development **144**, 1798 (2017).

[33] P. Campinho, M. Behrndt, J. Ranft, T. Risler, N. Minc, and C.-P. Heisenberg, Tension-oriented cell divisions limit anisotropic tissue tension in epithelial spreading during zebrafish epiboly, Nat. Cell Biol. **15**, 1405 (2013).

[34] A. Elosegui-Artola, The extracellular matrix viscoelasticity as a regulator of cell and tissue dynamics, Curr. Opin. Cell Biol. **72**, 10 (2021).

[35] J. G. Tidball, Energy stored and dissipated in skeletal muscle basement membranes during sinusoidal oscillations, Biophys. J. **50**, 1127 (1986).

[36] E. Fischer-Friedrich, Y. Toyoda, C. J. Cattin, D. J. Müller, A. A. Hyman, and F. Jülicher, Rheology of the active cell cortex in mitosis, Biophys. J. **111**, 589 (2016).

[37] O. Lieleg, M. M. A. E. Claessens, Y. Luan, and A. R. Bausch, Transient binding and dissipation in cross-linked actin networks, Phys. Rev. Lett. **101**, 108101 (2008).

[38] K. V. Iyer, R. Piscitello-Gómez, J. Paijmans, F. Jülicher, and S. Eaton, Epithelial viscoelasticity is regulated by mechanosensitive E-cadherin turnover, Curr. Biol. **29**, 578 (2019).

[39] M. Buszczak, S. Paterno, D. Lighthouse, J. Bachman, J. Planck, S. Owen, A. D. Skora, T. G. Nystul, B. Ohlstein, A. Allen *et al.*, The Carnegie Protein Trap Library: A versatile tool for *Drosophila* developmental studies, Genetics **175**, 1505 (2007).

[40] E. Frey, K. Kroy, and J. Wilhelm, Viscoelasticity of biopolymer networks and statistical mechanics of semiflexible polymers, Adv. Struct. Biol. **5**, 135 (1999).

[41] P. Agarwal and R. Zaidel-Bar, Principles of actomyosin regulation in vivo, Trends Cell Biol. **29**, 150 (2019).

[42] E. Izquierdo, T. Quinkler and S. De Renzis, Guided morphogenesis through optogenetic activation of Rho signalling during early *Drosophila* embryogenesis, Nat. Commun. **9**, 2366 (2018).

[43] L. Sui and C. Dahmann, Increased lateral tension is sufficient for epithelial folding in *Drosophila*, Development **147**, dev194316 (2020).

[44] H. Jiang and S. X. Sun, Cellular pressure and volume regulation and implications for cell mechanics, Biophys. J. **105**, 609 (2013).

[45] F. Lang, Mechanisms and significance of cell volume regulation, J. Am. Coll. Nutr. **26**, 613S (2007).

[46] A. A. Mongin and S. N. Orlov, Mechanisms of cell volume regulation and possible nature of the cell volume sensor, Pathophysiology **8**, 77 (2001).

[47] R. T. Miller, Mechanical properties of basement membrane in health and disease, Matrix Biol. **57-58**, 366 (2017).

[48] H. Li, Y. Zheng, Y. L. Han, S. Cai, and M. Guo, Nonlinear elasticity of biological basement membrane revealed by rapid inflation and deflation, Proc. Natl. Acad. Sci. USA **118**, e2022422118 (2021).

[49] A. J. Licup, S. Münster, A. Sharma, M. Sheinman, L. M. Jawerth, B. Fabry, D. A. Weitz, and F. C. MacKintosh, Stress controls the mechanics of collagen networks, Proc. Natl. Acad. Sci. USA **112**, 9573 (2015).

[50] A. Keller, F. Lanfranconi, and C. M. Aegerter, The influence of geometry on the elastic properties of the *Drosophila* wing disc, Physica A **510**, 208 (2018).

[51] S. Alt, P. Ganguly, and G. Salbreux, Vertex models: From cell mechanics to tissue morphogenesis, Philos. Trans. R. Soc. B **372**, 20150520 (2017).

[52] M. Mokbel, K. Hosseini, S. Aland, and E. Fischer-Friedrich, The Poisson ratio of the cellular actin cortex is frequency dependent, Biophys J. **118**, 1968 (2020).

[53] A. M. Howard, K. S. LaFever, A. M. Fenix, C. R. Scurrah, K. S. Lau, D. T. Burnette, G. Bhave, N. Ferrell, and A. Page-McCaw, DSS-induced damage to basement membranes is repaired by matrix replacement and crosslinking, J. Cell Sci. **132**, jcs.226860 (2019).

[54] T. Schluck, U. Nienhaus, T. Aegerter-Wilmsen, and C. M. Aegerter, Mechanical control of organ size in the development of the *Drosophila* wing disc, PLoS ONE **8**, e76171 (2013).

[55] G. Bhave, S. Colon, and N. Ferrell, The sulfilimine cross-link of collagen IV contributes to kidney tubular basement membrane stiffness, Am. J. Physiol.-Renal. **313**, F596 (2017).

[56] C. J. Chan, M. Costanzo, T. Ruiz-Herrero, G. Mönke, R. J. Petrie, M. Bergert, A. Diz-Muñoz, L. Mahadevan, and T. Hiiragi, Hydraulic control of mammalian embryo size and cell fate, Nature (London) **571**, 112 (2019).

[57] J.-L. Maître, R. Niwayama, H. Turlier, F. Nédélec, and T. Hiiragi, Pulsatile cell-autonomous contractility drives compaction in the mouse embryo, Nat. Cell Biol. **17**, 849 (2015).

[58] Q. Yang, S.-L. Xue, C. J. Chan, M. Rempfler, D. Vischi, F. Maurer-Gutierrez, T. Hiiragi, E. Hannezo, and P. Liberali, Cell fate coordinates mechano-osmotic forces in intestinal crypt formation, Nat. Cell Biol. **23**, 733 (2021).

[59] N. Khalilgharibi and Y. Mao, To form and function: On the role of basement membrane mechanics in tissue development, homeostasis and disease, Open Biol. **11**, 200360 (2021).

[60] Y. Matsubayashi, B. J. Sánchez-Sánchez, S. Marcotti, E. Serna-Morales, A. Dragu, M.-d.-C. Díaz de la Loza, G. Vizcay-Barrena, R. A. Fleck, and B. M. Stramer, Rapid homeostatic turnover of embryonic ECM during tissue morphogenesis, Dev. Cell **54**, 33 (2020).

[61] M. Tozluoğlu, M. Duda, N. J. Kirkland, R. Barrientos, J. J. Burden, J. J. Muñoz, and Y. Mao, Planar differential growth rates initiate precise fold positions in complex epithelia, Dev. Cell **51**, 299 (2019).

[62] R. F. Fisher, The significance of the shape of the lens and capsular energy changes in accommodation, J. Physiol. **201**, 21 (1969).

[63] H. Jin and J. L. Lewis, Determination of Poisson's ratio of articular cartilage by indentation using different-sized indenters, J. Biomech. Eng. **126**, 138 (2004).

[64] J. Candiello, M. Balasubramani, E. M. Schreiber, G. J. Cole, U. Mayer, W. Halfter, and H. Lin, Biomechanical properties of native basement membranes, FEBS J. **274**, 2897 (2007).

[65] A. T. Quiñones-Coello, L. N. Petrella, K. Ayers, A. Melillo, S. Mazzalupo, A. M. Hudson, S. Wang, C. Castiblanco, M. Buszczak, R. A. Hoskins *et al.*, Exploring strategies for protein trapping in *Drosophila*, Genetics **175**, 1089 (2007).

[66] D. Umetsu, B. Aigouy, M. Aliee, L. Sui, S. Eaton, F. Jülicher, and C. Dahmann, Local increases in mechanical tension shape compartment boundaries by biasing cell intercalations, Curr. Biol. **24**, 1798 (2014).

[67] G. Guglielmi, J. D. Barry, W. Huber, and S. De Renzis, An optogenetic method to modulate cell contractility during tissue morphogenesis, Dev. Cell **35**, 646 (2015).

[68] S. E. McGuire, P. T. Le, A. J. Osborn, K. Matsumoto, and R. L. Davis, Spatiotemporal rescue of memory dysfunction in *Drosophila*, Science **302**, 1765 (2003).

[69] A. J. Booth, G. B. Blanchard, R. J. Adams, and K. Röper, A dynamic microtubule cytoskeleton directs medial actomyosin function during tube formation, Dev. Cell **29**, 562 (2014).

[70] M. Rauzi, P.-F. Lenne, and T. Lecuit, Planar polarized actomyosin contractile flows control epithelial junction remodelling, Nature (London) **468**, 1110 (2010).

[71] J. Schindelin, I. Arganda-Carreras, E. Frise, V. Kaynig, M. Longair, T. Pietzsch, S. Preibisch, C. Rueden, S. Saalfeld, B. Schmid *et al.*, Fiji: An open-source platform for biological-image analysis, Nat. Methods **9**, 676 (2012).

[72] M. Weigert, U. Schmidt, T. Boothe, A. Müller, A. Dibrov, A. Jain, B. Wilhelm, D. Schmidt, C. Broaddus, S. Culley *et al.*, Content-aware image restoration: Pushing the limits of fluorescence microscopy, Nat. Methods **15**, 1090 (2018).

[73] B. Aigouy, R. Farhadifar, D. B. Staple, A. Sagner, J.-C. Röper, F. Jülicher, and S. Eaton, Cell flow reorients the axis of planar polarity in the wing epithelium of *Drosophila*, Cell **142**, 773 (2010).

[74] K.-T. Wan, S. Guo, and D. A. Dillard, A theoretical and numerical study of a thin clamped circular film under an external load in the presence of a tensile residual stress, Thin Solid Films **425**, 150 (2003).

[75] C. Lee, X. Wei, J. W. Kysar, and J. Hone, Measurement of the elastic properties and intrinsic strength of monolayer graphene, Science **321**, 385 (2008).

[76] D. Vella, A. Ajdari, A. Vaziri, and A. Boudaoud, Indentation of ellipsoidal and cylindrical elastic shells, Phys. Rev. Lett. **109**, 144302 (2012).

[77] I. N. Sneddon, The relation between load and penetration in the axisymmetric Boussinesq problem for a punch of arbitrary profile, Int. J. Eng. Sci. **3**, 47 (1965).

[78] Y. M. Efremov, W.-H. Wang, S. D. Hardy, R. L. Geahlen, and A. Raman, Measuring nanoscale viscoelastic parameters of cells directly from AFM force-displacement curves, Sci. Rep. **7**, 1541 (2017).

[79] N. Phan-Thien, *Understanding Viscoelasticity: An Introduction to Rheology* (Springer, Berlin, Heidelberg, 2012).

[80] A. Y. Malkin and A. I. Isayev, 2: Viscoelasticity, in *Rheology Concepts, Methods, and Applications*, 2nd ed., edited by A. Y. Malkin and A. I. Isayev (Elsevier, Oxford, UK, 2012), pp. 43–126.

[81] https://gitlab.com/polffgroup/wingdiscafmindentation